



Research paper

Unifying the contact in signed distance field-based and conventional discrete element methods

Zhengshou Lai ^{a,b,c}, Y.T. Feng ^d, Jidong Zhao ^{e,f}, Linchong Huang ^{a,b,c,*}

^a School of Civil Engineering, Sun Yat-sen University, Guangzhou 510275, China

^b State Key Laboratory for Tunnel Engineering, Guangzhou, 510275, China

^c Guangdong Key Laboratory of Marine Civil Engineering, School of Civil Engineering, Sun Yat-sen University, Guangzhou 510275, China

^d Zienkiewicz Centre for Computational Engineering, College of Engineering, Swansea University, UK

^e Department of Civil and Environmental Engineering, The Hong Kong University of Science and Technology, Hong Kong, China

^f HKUST Shenzhen-Hong Kong Collaborative Innovation Research Institute, Shenzhen 518045, China

ARTICLE INFO

Keywords:

Discrete element method
Signed distance field
Irregular shape
Contact
Contact parameter

ABSTRACT

The signed distance field-based discrete element method (SDF-DEM) has demonstrated significant success in various applications; however, a key challenge hindering its widespread adoption lies in the establishment of its connection with conventional contact models. To address this challenge, this study introduces two formulations of contact potential within SDF-DEM, drawing analogies to both linear and Hertzian contact models. Comprehensive relationship between the parameters of the proposed contact potentials of SDF-DEM and those of conventional contact models is established. The energy conservation characteristic of SDF-DEM is verified through a two-particle colliding and bouncing test, and the critical timestep issue is investigated and addressed. Discrete element simulations are conducted for a triaxial compression test and a rockfall test, involving both spherical particles and general irregularly shaped particles. The results underscore the accuracy and numerical stability of the SDF-DEM with the developed potential models. This work is anticipated to contribute not only to advancing the understanding of SDF-DEM and the potential-based contact theory but also to providing robust framework that bridges the gap of SDF-DEM with conventional models.

1. Introduction

Granular materials play a ubiquitous role in both natural and industrial settings, presenting significant computational challenges due to their intricate behavior (Cho et al., 2006; Shi et al., 2021). The discrete element method (DEM) (Cundall and Strack, 1979) has emerged as a pivotal tool for modeling the microscopic dynamics of individual particles and unraveling the collective behavior of granular assemblies. However, accurately representing irregular particle shapes within DEM remains an ongoing challenge, prompting the development of innovative techniques such as the level-set discrete element method (LS-DEM) (Kawamoto et al., 2016, 2018) and the signed-distance-field discrete element method (SDF-DEM) (Lai et al., 2022). The SDF-DEM, a superset variant of LS-DEM,¹ addresses this challenge by utilizing a signed distance function for particle shape description. This allows SDF-DEM to effectively represent virtually any morphology. The versatility of SDF-DEM has led to its application in a diverse range of scenarios,

including the column collapse of porous coral sand (Huang et al., 2023), triaxial compression tests of Martian-like soil (Kawamoto et al., 2016), structural response of building blocks (Harmon et al., 2020; Zhou et al., 2023), tunable mechanical properties of structured fabrics (Wang et al., 2021), breakage and non-uniform basal melt of sea ice floes (Moncada et al., 2023), etc.

SDF-DEM employs a node-to-surface algorithm for detecting contacts between particles, and defines contact forces at each penetrating node. As outlined by van der Haven et al. (2023), SDF-DEM (or LS-DEM) encompasses three approaches for computing inter-particle forces based on the penetration distance of surface nodes: the single-node approach (Li et al., 2019), the multiple-nodes-averaged approach (Wang and Ji, 2022), and the multiple-nodes-summed approach (Kawamoto et al., 2016, 2018; Lai et al., 2022). In the single-node approach, only the deepest-penetrating node is considered (Li et al., 2019). However, this approach exhibits undesirable properties, including (1) an identical contact force for contacts with the same penetration depth but

* Corresponding author.

E-mail address: hlinch@mail.sysu.edu.cn (L. Huang).

¹ SDF-DEM, can be regarded as a superset of LS-DEM, employing a broad-sense signed distance function to describe particle shape. The contact behavior is derived from a contact potential function in an energy-conserving manner. SDF-DEM converges to LS-DEM when using a discrete level set for the signed distance function.

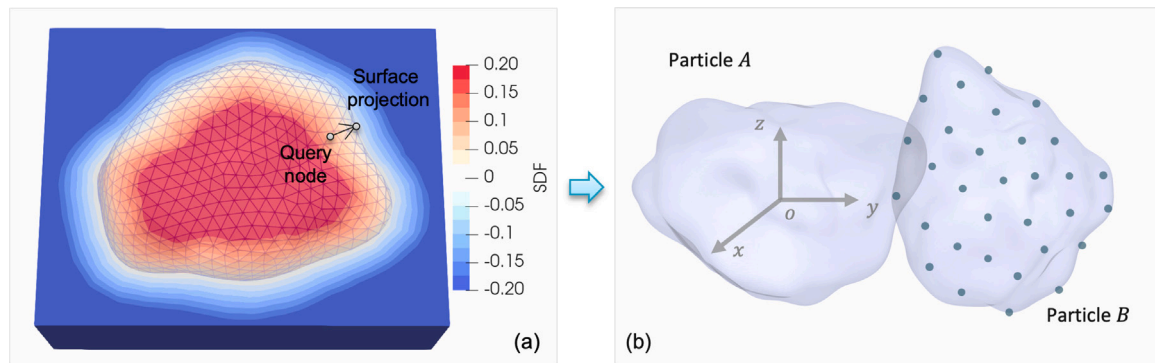


Fig. 1. Illustration of the SDF-DEM approach: (a) particle described by SDF, and (b) the node-to-surface algorithm for contact detection.

different widths; and (2) discontinuities in the force. These issues can lead to stability concerns and violate elastic energy conservation. The multiple-nodes-averaged approach addresses the aforementioned problems by averaging the contact forces of all penetrating nodes (Wang and Ji, 2022). While it ensures continuous contact point positions in the limit of using infinite nodes, this approach introduces challenges such as non-monotonic force increases due to varying surface-to-volume ratios. This variability can result in path-dependent elastic energy and instability, particularly under strain-controlled conditions. The multiple-nodes-summed approach, involving the summation of forces of all penetrating nodes, potentially offers stable simulations while conserving elastic energy (Lai et al., 2022). This approach is widely adopted in the literature (Kawamoto et al., 2016, 2018; Lai et al., 2022) for its ability to provide stable and reliable results across various scenarios.

However, the multiple-nodes-summed approach in SDF-DEM exhibits a critical limitation: its contact behavior is significantly influenced by the discretization of surface nodes, as highlighted in Duriez and Bonelli (2021), Feldfogel et al. (2023) and van der Haven et al. (2023). This limitation becomes particularly pronounced for highly compressible problems, leading to a divergence in the response with discretization refinement. To address this issue, Feldfogel et al. (2023) have proposed a methodologically rigorous and computationally efficient formulation for the contact model. The adapted formulation adopts the classical contact description from continuum mechanics, where contact interactions are traction-based. In this strategy, each node is associated with a tributary area, and the total contact force is determined through an area-weighted summation of the forces from all penetrating nodes. This modification effectively mitigates the discretization-divergence issue, thereby providing a more robust and reliable solution, especially in scenarios involving highly compressible materials.

Another noteworthy solution to the discretization issue of the conventional LS-DEM is the volume-interacting level-set discrete element method (VLS-DEM) (van der Haven et al., 2023). Departing from the use of surface nodes for computing inter-particle forces, VLS-DEM introduces an octree integration algorithm (OIA). This algorithm determines the overlap volume, contact point, interaction normal, and contact surface area between two contacting particles. The methodology of VLS-DEM effectively addresses the limitations of LS-DEM, enhancing physical consistency and the ability to handle arbitrary particle shapes. Notably, VLS-DEM can be considered as a concrete implementation of the contact volume-based energy-conserving contact theory initially proposed by Feng (2021a,b). This innovative approach represents a significant advancement in simulating granular materials, offering improved accuracy and versatility in capturing complex interactions between particles.

Despite the strides made in addressing discretization issues, a significant challenge still impedes the widespread application of SDF-DEM. This challenge revolves around establishing connections between the

method and conventional contact models, such as the linear-spring contact model (Cundall and Strack, 1979; Thornton et al., 2011) and the Hertzian contact model (Hertz, 1882; Johnson, 1987; Di Renzo and Di Maio, 2005). Researchers have accumulated substantial knowledge and experience regarding the contact parameters and corresponding behavior of these conventional models (Malone and Xu, 2008; Rojek et al., 2012; Coetzee, 2017; Rackl and Hanley, 2017; Mudarisov et al., 2022). Moreover, analytical or empirical functions for the critical timestep (Otsubo et al., 2017; Tu and Andrade, 2008; Hart et al., 1988; Thornton, 2000; Li et al., 2005), crucial for ensuring the numerical stability of DEM simulations, have been developed for conventional contact models. However, when it comes to SDF-DEM (or LS-DEM), this wealth of knowledge and experience is not directly transferable, which constrains its broader application. The absence of a seamless connection with well-established contact models poses a barrier to the widespread adoption of SDF-DEM, limiting its utility in scenarios where the familiarity and predictability of conventional models are crucial.

The primary contribution of this paper lies in the effort to unify the contact behaviors in signed distance field-based and conventional discrete element methods. Two formulations of contact potential are introduced, drawing analogies to the linear contact model and the Hertzian contact model, respectively. Furthermore, a comprehensive relationship is established between the parameters of the proposed contact potential models in SDF-DEM and those of conventional contact models. These contributions bridge the gap between the energy-conserving contact theory in SDF-DEM and the conventional models. The current work also provides the theoretical coherence of the approach and offers a practical pathway for the broader application of SDF-DEM.

2. The SDF-DEM framework

For the sake of discussion, this section presents a brief description of the SDF-DEM framework. Interested readers are referred to Lai et al. (2022) for more details. In the SDF-based DEM, particles are defined by a signed distance function (SDF), denoted as $\Phi(\vec{x})$. This function maps a spatial point \vec{x} in \mathcal{R}^3 to a signed distance value d . Unlike conventional SDF, which typically represents the shortest distance from a point to a particle surface, SDF-DEM adopts a broader definition. It allows the SDF to be the shortest distance, radial distance, or any distance satisfying the condition that SDF isosurfaces are non-self-intersecting. Assuming that SDF is positive inside a particle and negative outside, with the zeroth isosurface representing the particle surface, an example of SDF-based representation is illustrated in Fig. 1(a). The SDF-based particle model includes a surface projection function that projects a point inside a particle onto the particle surface, as shown in Fig. 1(a). This function is crucial for determining contact points, essential in evaluating contact forces and moments within contact models.

In the SDF-based DEM, the node-to-surface contact algorithm, as depicted in Fig. 1(b), is employed for contact detection and resolution.

The surface of Particle B is discretized into surface nodes, and contact detection involves checking whether any node on Particle B intrudes into Particle A . A dual approach is utilized for contact resolution. The contact normal force is evaluated using the energy-conserving contact theory proposed by Feng (2021a). At the same time, the tangential frictional contact force is determined employing the classical linear contact model with the Coulomb's law of friction. Note that the contact normal force is derived from the derivatives of a contact potential function $w(\vec{x}, \vec{\theta})$ with respect to the relative translation and rotation of the two contacting particles. Mathematically, this is expressed as:

$$\vec{F}_n = -\frac{\partial w(\vec{x}, \vec{\theta})}{\partial \vec{x}} \quad (1)$$

$$\vec{M}_n = -\frac{\partial w(\vec{x}, \vec{\theta})}{\partial \vec{\theta}} \quad (2)$$

$$w(\vec{x}, \vec{\theta}) = \sum_{N_i \in B \rightarrow A} F(d_i(\vec{x}, \vec{\theta})) \quad (3)$$

where $N_i \in B \rightarrow A$ denotes the intruding nodes; \vec{F}_n and \vec{M}_n represent the contact normal force and moment, respectively, while $w(\vec{x}, \vec{\theta})$ denotes the total contact potential and $F(d_i(\vec{x}, \vec{\theta}))$ represents the contact potential associated with each penetrating node. The variables \vec{x} and $\vec{\theta}$ represent the relative position and rotation of Particle B with respect to Particle A . This methodology ensures a robust and physically consistent approach to resolving normal and tangential forces during particle interactions.

3. Linear contact potential: analogy of the linear contact model

3.1. Preliminary: integration of contact volume

For a given contact configuration, as illustrated in Fig. 2, the contact volume, representing the intersection volume of the two particles, can be expressed as:

$$V = \int_{\Omega} h \, d\Omega \quad (4)$$

where h denotes the height of the cap, and Ω represents the contact hyper-plane. Here, it is assumed that the surface intersection of the two particles forms a hyper-plane, and that each point on the intersecting surfaces can be projected onto the hyper-plane, similar to the case of two contacting spheres. The height of the cap is thus the projection distance of the two points with the same projection. Obtaining a closed-form solution for this integration is often impractical, particularly for complex particle surfaces. Therefore, following the concept of the node-based representation of particle surfaces, it is reasonable to approximate the contact volume discretely:

$$V \approx \sum_{N_i \in B \rightarrow A} S_i d_i \cos \alpha_i \quad (5)$$

where S_i is the discretized integration surface associated with node N_i , d_i is the intrusion depth, and α_i is the cross angle between the intrusion depth direction and the cap height direction.

3.2. Formulation of contact potential

Using the contact volume formulation and inspired by the contact-volume-based contact model by Feng (2021b), the contact potential can be defined as a linear function of the contact volume:

$$F(d_i) = k_i S_i d_i \cos \alpha_i \approx k_i S_i d_i \quad (6)$$

where k_i is a stiffness parameter associated with each node. In practical applications, the discretized integration surface S_i can be computed in advance and remains constant. For simplicity, it can also be approximated as the total surface area S_B averaged over each node (i.e., S_B/N_B), assuming uniformly distributed surface nodes. In DEM,

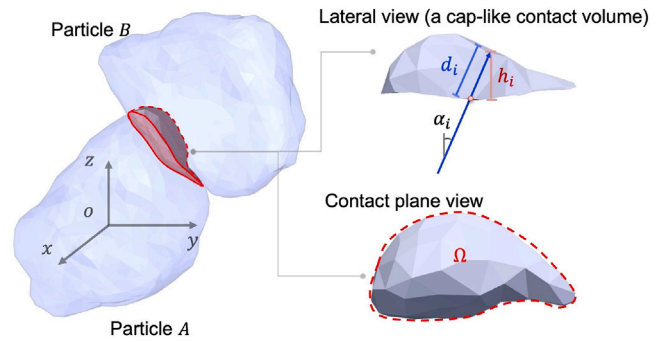


Fig. 2. Integration of contact volume between two particles in contact.

the contact overlap and area are usually very small. It thus becomes reasonable to approximate the cap height with the intruding depth to establish a closed-form formulation of the contact volume. As a result, the cross angle α_i is close to 0, and the term $\cos \alpha_i$ can be approximated as 1. Consequently, with recourse to Eq. (1) the contact normal force at each intruding node can be expressed as:

$$\vec{F}_{n,i} = -k_i S_i \frac{\partial d_i}{\partial \vec{x}} \quad (7)$$

The total contact normal force \vec{F}_n can be obtained (at the particle center) as the summation of the contact normal forces at all intruding nodes. Note that in the current node-wise approach, the contact moment $\vec{M}_{n,i}$ associated with each intruding node is zero: $\vec{M}_{n,i} = 0$. However, a resulting contact moment \vec{M} can be obtained at the particle center by assembling the moments produced by all $\vec{F}_{n,i}$.

It is important to note that Eq. (7) may lead to a non-continuous total force in a discrete fashion, resulting in a stair-like force-displacement profile. This stair-like profile can be a major contributor to numerical instability in DEM simulations. To address this issue and to achieve a smooth and continuous force-displacement profile, a robust scheme is proposed by incorporating a sigmoid function of the intrusion depth d_i . The contact potential and contact normal force are thus modified as follows:

$$F(d_i) = k_i S(d_i) S_i d_i \quad (8)$$

$$\vec{F}_{n,i} = -k_i S_i \frac{\partial (S(d_i) d_i)}{\partial \vec{x}} \quad (9)$$

where $S(d_i)$ is a sigmoid function satisfying $S(0) = 0$ and $S(d_{i,\max}) = 1$, in which $d_{i,\max}$ denotes the maximum permissible intrusion depth during a collision event. As a small contact overlap region is normally assumed in DEM, $d_{i,\max}$ is typically less than 5% of the particle size. The sigmoid function ensures that the contact volume associated with the intruding node N_i from Particle B is considered to be zero when the node just starts to penetrate into Particle A ($d_i = 0$) and becomes a unit when the intrusion depth becomes significant ($d_i = d_{i,\max}$). In this work, the following algebraic formulation of the sigmoid function is adopted due to its computational efficiency:

$$S(d_i) = \frac{cd_i/d_B}{\sqrt{1 + (cd_i/d_B)^2}} \quad (10)$$

where c is a constant parameter controlling the shape of the function, estimated as $c = 100$, and d_B is the equivalent size (diameter of a sphere of equal-volume) of Particle B . With $c = 100$, S is evaluated as 0.92 with a d_i/d_B of 0.025 (i.e., contact overlap is 2.5% of particle size) and 0.98 for 0.05. In practice, $d_{i,\max}$ could be estimated from the expected confining pressure and equivalent stiffness of each particle.

Substituting Eq. (10) into Eq. (9), the contact normal force can be explicitly calculated. Typically, for particle models such as ellipsoid, quatics, level set, etc. Lai et al. (2022), a closed and explicit form of the partial derivative term in Eq. (9) can be analytically derived from

the specific formulation of SDF. In this work, to facilitate a generic implementation of the contact solver, the partial derivative term is instead numerically approximated using the finite difference approach by translating Particle B with a tiny displacement in each dimension.

3.3. Connection with conventional linear contact model

From a practical perspective, it is of interest to establish a relationship between the stiffness parameter k_i and the conventional contact normal stiffness k_n . Given that the proposed linear contact potential is analogous to the contact volume-based contact model, it has been demonstrated in Feng (2021b) that the stiffness parameter k_i can be related to the contact normal stiffness k_n of the linear contact model by

$$k_i = k_n / (\pi d_B C_{sr}) \quad (11)$$

where $C_{sr} = d_A / (d_A + d_B)$ is a coefficient to account for the size ratio of the two particles in contact. It is important to note that this relationship is derived from the case of spherical particles and may exhibit some deviation for irregularly shaped particles. For a more accurate approximation in the case of irregularly shaped particles, d_A and d_B can be replaced by twice the radius of curvature at the contact point.

3.4. Critical timestep

In typical DEM codes, particle velocity and position are updated using the velocity Verlet or central difference algorithm (Belytschko et al., 1979; Martyts and Mountain, 1999). This algorithm is only conditionally stable, meaning that the timestep should be less than a threshold, known as the critical timestep (O'Sullivan and Bray, 2004; Otsubo et al., 2017). Using a timestep greater than the critical timestep may lead to excessive particle movement in one time increment, resulting in artificially large overlaps and contact forces.

Various approaches exist to estimate the critical timestep for DEM simulations, as summarized and assessed in O'Sullivan and Bray (2004) and Otsubo et al. (2017). One commonly used approximation for the critical timestep, originally proposed by Cundall and Strack (1979), is given by

$$\Delta t_{\text{crit}} = \sqrt{\frac{m}{k_n}} \quad (12)$$

where m represents the particle mass, and k_n is the equivalent contact normal stiffness. It is important to note that Eq. (12) provides an approximation of the critical timestep for a single contact and is not a conservative estimate. In Hart et al. (1988), a suggestion is made to multiply the critical timestep calculated from Eq. (12) by a user-specified parameter α (typically between 0.1 and 0.2) to account for the presence of multiple contacts and also for the solution accuracy.

4. Three-halves-power contact potential: analogy to Hertzian contact model

4.1. Formulation of contact potential

We begin by considering spherical particles to establish a connection between the three-halves-power contact potential and the conventional Hertzian contact model. Referring to the formulation of the nodal distance-potential based energy-conserving contact theory defined in Eq. (1), the contact normal force is calculated as

$$\bar{F}_n = - \sum_{N_i}^{N_i \in B \rightarrow A} F'(d_i) \frac{\partial d_i}{\partial \bar{x}} \quad (13)$$

For the case of spherical particles, we approximate two key terms: the number of intruding nodes N_i and the partial derivative term $\frac{\partial d_i}{\partial \bar{x}}$. Illustrated in Fig. 3, for two identical spherical particles with a

penetration depth of δ_n , the area of the contact surface S_c can be approximated as $S_c = \pi d_B \delta_n C_{sr}$. Consequently, the number of intruding nodes can be approximated as $\pi d_B \delta_n C_{sr} / \bar{S}_i$, where \bar{S}_i is the average surface area associated with each node, assuming that surface nodes are uniformly distributed. In addition, for a small contact, the partial derivative term $\frac{\partial d_i}{\partial \bar{x}}$ can be approximated as a unit, based on the contact configuration depicted in Fig. 3. Thus, the contact normal force given by Eq. (13) can be further approximated as

$$F_n = -\beta \frac{\pi d_B C_{sr}}{\bar{S}_i} \delta_n F'(\bar{d}) \quad (14)$$

where \bar{d} represents the average intrusion depth d_i of all intruding nodes, and β is a parameter introduced to account for the difference due to using $F'(\bar{d})$ to approximate $F'(d_i)$. Eq. (14) suggests that if $F'(\bar{d})$ is in the order of $\delta_n^{1/2}$, the resulting contact normal force is likely to be proportional to $\delta_n^{3/2}$, a characteristic feature of the Hertzian contact model.

In light of this analysis, we propose a three-halves-power contact potential given by

$$F(d_i) = \frac{2}{3} k_i S_i d_i \sqrt{d_i / d_B} \quad (15)$$

where k_i is a stiffness related model parameter. Consequently, the contact normal force at each intruding node can be expressed as

$$\bar{F}_{n,i} = -k_i S_i \sqrt{d_i / d_B} \frac{\partial d_i}{\partial \bar{x}} \quad (16)$$

As with the linear contact potential case, the partial derivative will be computed using the finite difference approach in implementation.

4.2. Connection with conventional Hertzian contact model

Recalling the Hertzian contact model, the contact normal force is calculated as

$$F_n = \frac{4}{3} E^* R^{*1/2} \delta_n^{3/2} \quad (17)$$

where E^* is the equivalent Young's modulus calculated as $1/E^* = (1 - \nu_A^2) / E_A + (1 - \nu_B^2) / E_B$, where ν is the Poisson's ratio, and E is the Young's modulus. R^* is the equivalent particle radius calculated as $1/R^* = 1/R_A + 1/R_B$, where R is the particle radius or radius of curvature at the contact point, and subscripts A and B denote the two particles.

By comparing Eq. (17) with Eq. (14), the relation between the stiffness parameters k_i , E^* , and R^* can be obtained as

$$k_i = \frac{4E^* \sqrt{R^*}}{3\pi\beta C_{sr} \sqrt{d_B}} \quad (18)$$

where β is the empirical parameter accounting for the error due to the approximation in d_i , \bar{d} , and δ_n . Based on single-contact simulations (to be presented in the subsequent section), a suitable value for β is found to be 0.65, providing a good agreement between the proposed three-halves-power contact potential-based contact theory and the Hertzian contact model for the case of spherical particles.

4.3. Critical timestep

Recalling the Hertzian contact model given by Eq. (17), the transient translation contact normal stiffness can be calculated as

$$k_n = \frac{4}{3} E^* \sqrt{R^*} \delta_n \quad (19)$$

By utilizing Eq. (18), the transient translation contact normal stiffness of the three-halves-power contact potential-based contact model can be estimated as

$$k_n = \pi\beta C_{sr} k_i \sqrt{d_B \delta_n} \quad (20)$$

To clarify, d_B is the equivalent particle size, k_i is the stiffness-related model parameter, δ_n is the penetration depth, and β is an empirical

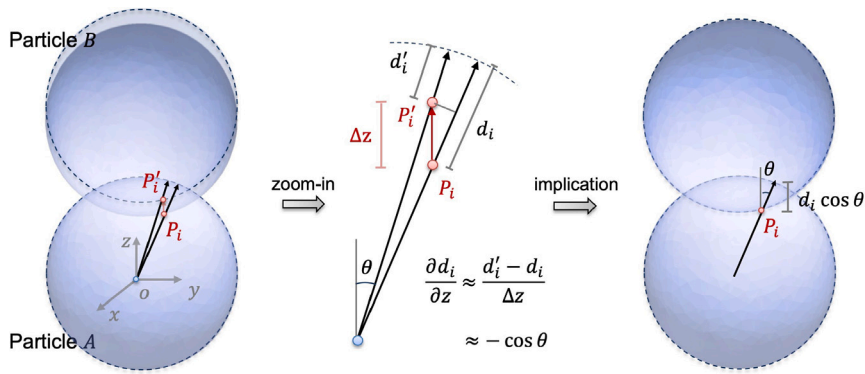


Fig. 3. Illustration of the contact between spheres and the partial derivative of the intrusion depth with respect to the normal of contact plane.

parameter with a recommended value of 0.65. In this context, δ_n can be approximated as the average penetration depth of all intruding nodes, specifically in the case of star-shaped particles. The critical timestep can then be estimated using Eq. (12).

5. Numerical examples

This section presents four numerical examples to verify and validate the proposed models. The examples include a static contact test between two particles to analyze force–displacement profiles; a dynamic contact test within a box container to assess energy conservation and explore critical timestep issues; a triaxial compression test on spherical particles to benchmark against conventional DEM; and a rockfall test on an irregularly shaped particle to study the impact of contact stiffness and surface node configurations. These examples collectively evaluate the effectiveness, accuracy, and robustness of the developed contact potential models within the SDF-DEM framework for different scenarios.

5.1. Force–displacement profile test

In the contact test shown in Fig. 4, Particle A is anchored at the origin, while Particle B is positioned on the top of Particle A with their centroids aligned along the z axis. The contact is initiated as Particle B moves downwards, resulting in increased penetration into Particle A. Both particles are of unit size, and their surfaces are discretized into a fixed number of uniformly distributed nodes using a radial distance-based weighted spherical centroidal Voronoi tessellation (Lai et al., 2022). For the reference case, the number of surface nodes is set to be 1000, and the sensitivity of the force–displacement profile to the number of surface nodes is investigated. The stiffness parameter k_i is arbitrarily chosen to be 1.0 N/m² for the sake of generality. Noted that friction and damping are not considered in the contact test. The initial study focuses on a contact test between two spherical particles as a verification case. Subsequently, irregularly shaped particles are considered and modeled using spherical harmonics. Spherical harmonics have become a prevalent method for modeling and characterizing irregularly shaped particles in various fields, such as industrial and geotechnical (Mollon and Zhao, 2014; Zhou et al., 2015; Zhou and Wang, 2017; Zhou et al., 2018). Readers interested in different particle models, including ellipsoid, quadrics, spherical harmonics, level set, polyhedron, etc., are referred to the original work on SDF-DEM (Lai et al., 2022).

5.1.1. Sphere case

For spheres with the linear contact case, Fig. 5(a) illustrates the magnitude of the contact normal force with the increasing normal displacement. The normal displacement is computed as the sum of the two particle radii minus the distance between the centroids of the

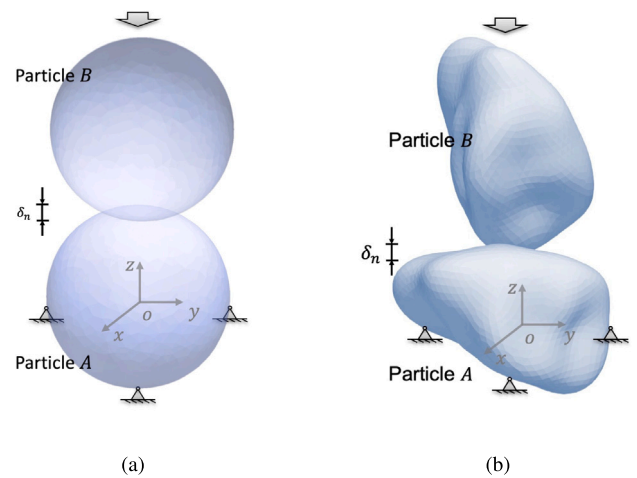


Fig. 4. Setup of the single contact test: (a) spherical case, and (b) irregularly shaped case.

two particles, representing the theoretical penetration depth of two spherical particles. As the normal displacement increases, the number of intruding nodes shows discrete increments. The contact normal force demonstrates a monotonically increasing behavior but with a variable rate of increase. The slight fluctuation in the increasing rate is a consequence of the sigmoid function, which prevents the force–displacement profile from resembling a stair-like pattern, as observed in Fig. 5(b). Overall, the force–displacement profile exhibits a roughly linear trend, closely resembling the theoretical results of the conventional linear contact model for spherical particles.

The main parameters in the proposed linear and three-halves contact potentials include the equivalent particle size d_B , the nodal surface area S_i , the stiffness-related parameter k_i , and an empirical constant c for the sigmoid function. The first two are determined by the colliding particles and the surface discretization, while the stiffness-related parameter k_i is adjustable to account for the material stiffness of the particles. To investigate how variations in these model parameters affect the simulation results, additional contact tests were conducted using different values of k_i and c . Fig. 6 presents the force–displacement profiles for the linear contact test with different stiffness parameters. As expected, the force–displacement profiles exhibit consistent parallel trends in the log–log scale plots across different values of k_i , indicating predictable behavior when k_i is linearly introduced into the contact potential formulation. Fig. 7 displays the force–displacement profiles for the linear contact test with different values of c . For small values of c , the contact normal force is lower than the analytical values, while larger values of c cause more fluctuations in

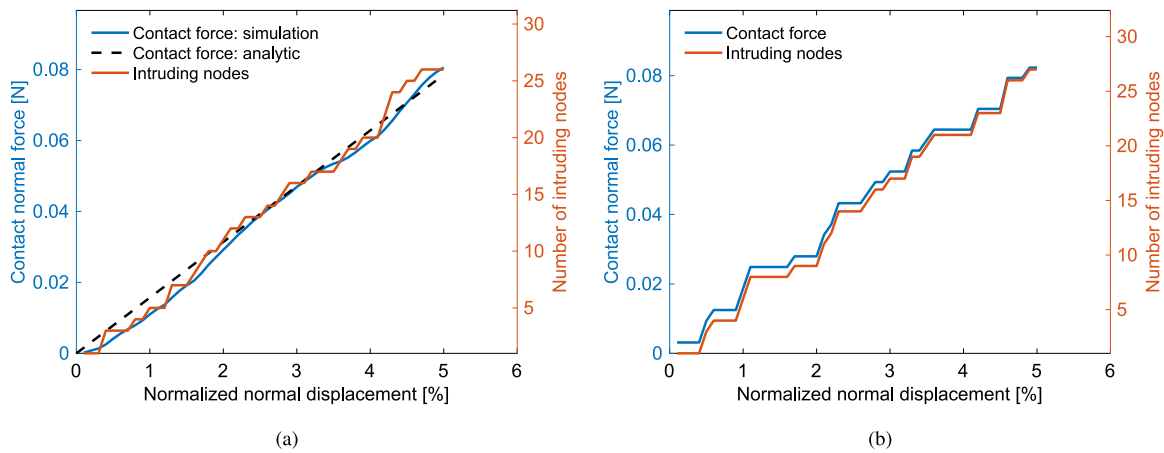


Fig. 5. Force–displacement profiles of the sphere and linear case of contact test (a) with sigmoid function and (b) without sigmoid function. The analytical result corresponds to the conventional linear contact model with an equivalent contact normal stiffness k_n of 1.57 N/m evaluated from Eq. (11).

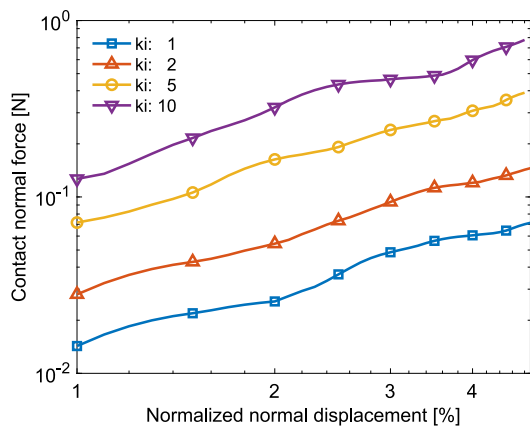


Fig. 6. Force–displacement profiles of the sphere and linear case of contact test with different stiffness parameters k_i .

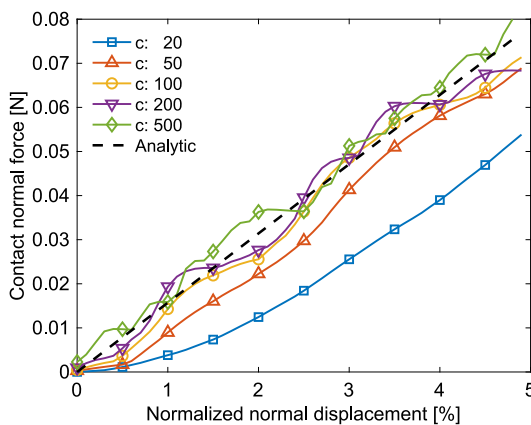


Fig. 7. Force–displacement profiles of the sphere and linear case of contact test with different constant parameters c in the introduced sigmoid function for the linear contact potential.

the force–displacement profiles. A value of 100 for c yields a reasonably smooth force–displacement profile, closely matching the expected linear contact behavior.

In SDF-DEM, the discretization of particle surfaces relies on surface nodes, where contact forces are defined. Consequently, the force–displacement profile can be influenced by the number of surface nodes

and the randomness in their configuration. To explore this influence, the contact test is performed in ten independent simulations, each featuring a distinct random configuration of surface nodes. The results, as depicted in Fig. 8(a), show slight discrepancies among the force–displacement profiles due to different configurations of surface nodes. Increasing the number of surface nodes can reduce such discrepancies. Fig. 8(b) presents the force–displacement results for different numbers of surface nodes. Notably, the force–displacement profile exhibits more significant variations at 500 surface nodes, but becomes less pronounced as the number of surface nodes increases to 1000 and beyond. This overall consistency in the force–displacement profiles across different numbers of surface nodes underlines the good discretization convergence characteristic of the linear contact potential model for SDF-DEM.

For the Hertzian contact case, the force–displacement profile is illustrated in Fig. 9(a), while Fig. 9(b) displays the results from ten different random sets of surface nodes. In contrast to the linear contact case, the force–displacement profile exhibits a smoother increasing rate. Although there are some variations between the results of ten different simulations, the overall agreement is good. The force–displacement profiles are best fitted by a power function with an exponent of about 1.49. This suggests that the proposed three-halves-power contact potential can accurately reproduce the characteristic features of the Hertzian contact. The force–displacement profiles of SDF-DEM and the conventional Hertzian contact model align well, conforming the developed relationship (Eq. (18)) between the parameters in the SDF-based contact potential model and the conventional Hertzian contact model.

5.1.2. Irregularly shaped case

For irregularly shaped particles modeled by spherical harmonics, similar to the sphere case, contact tests are conducted, as outlined in Fig. 4(b). In this scenario, due to the absence of analytical formulations for the contact normal displacement, the intrusion depth between particles is employed to quantify the contact normal displacement. It is calculated as the displacement of Particle B concerning its reference position when it is immediately in contact with Particle A . Fig. 10(a) displays the force–displacement profile for one contact test, while Fig. 10(b) shows the results from ten different random sets of surface nodes. In the force–displacement profile, both the contact normal force and the number of intruding nodes increase monotonically with the intrusion depth. However, the force–displacement profile exhibits slightly greater sigmoid-like fluctuations and an overall smaller increasing rate (equivalent contact normal stiffness) compared to the spherical case. These fluctuations and reduced contact stiffness are primarily due to the effects of shape irregularity. It is important to note that the proposed

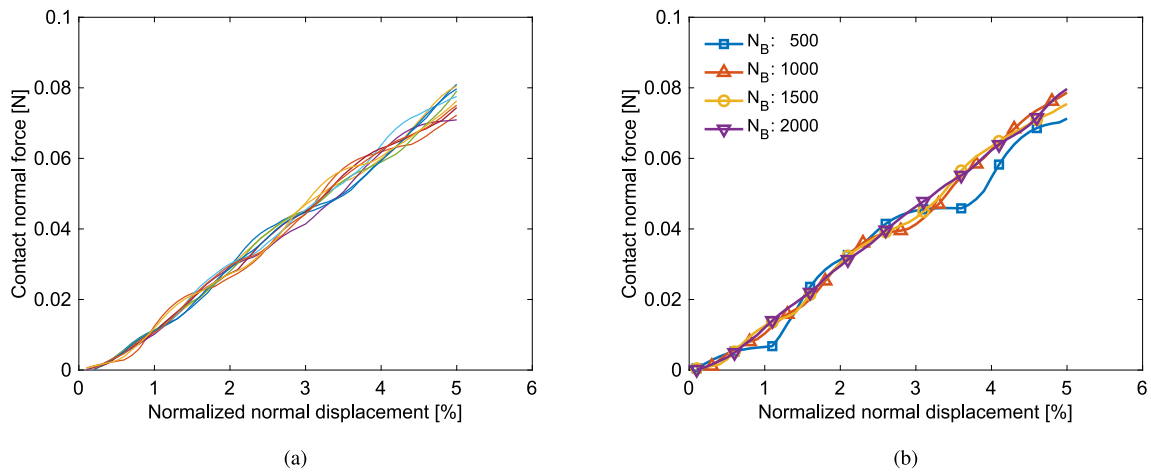


Fig. 8. Force–displacement profiles of the sphere and linear case of contact test for (a) ten different random sets of surface nodes and (b) different number of surface nodes.

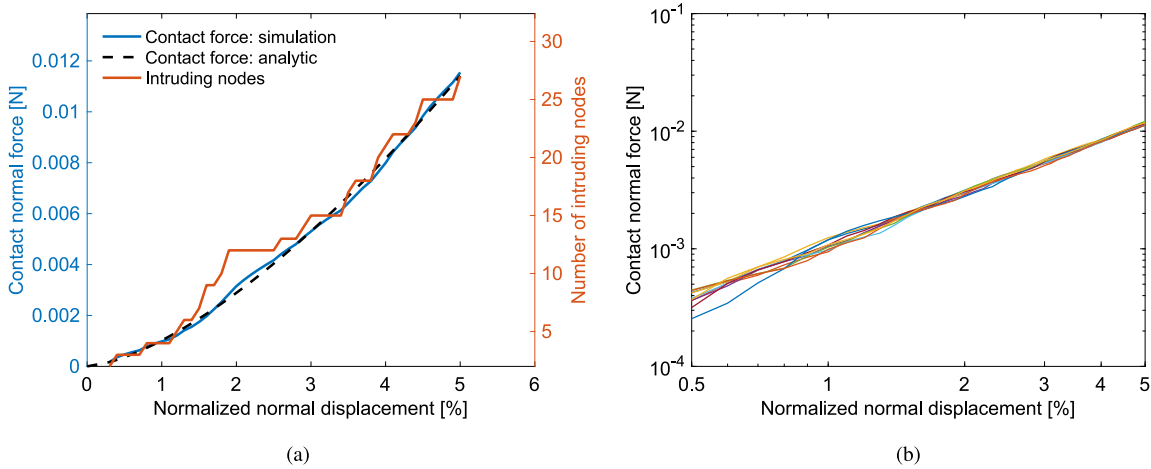


Fig. 9. Force–displacement profiles of the sphere and Hertzian case of contact test (a) in comparison with the theoretical results and (b) for ten different random sets of surface nodes. The analytical results corresponds to the convectonal Hertzian contact model with an equivalent Young’s modulus E^* of 1.53 Pa evaluated from Eq. (18).

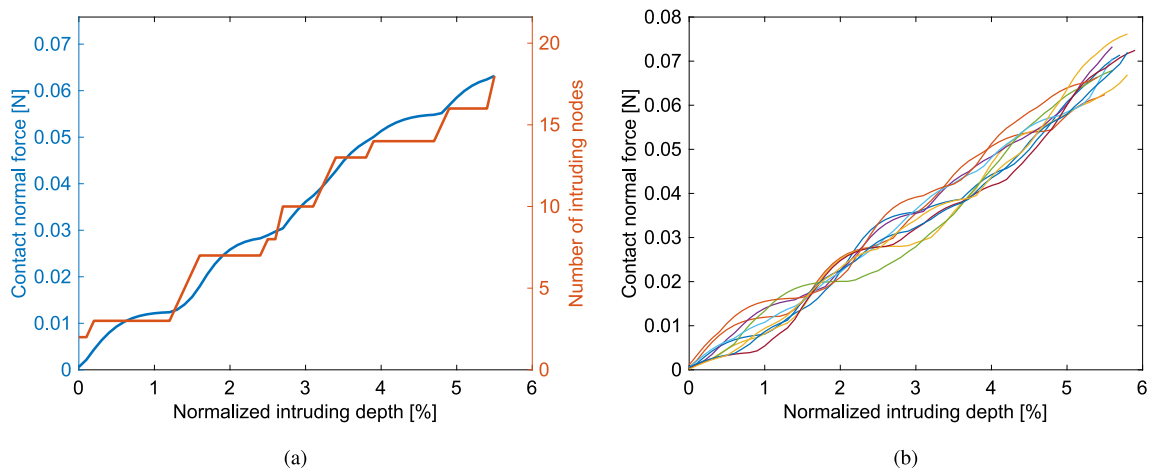


Fig. 10. Force–displacement profiles of the irregularly shaped and linear case of contact test (a) and the results of ten different random sets of surface nodes (b).

linear contact potential is not designed to precisely replicate the contact force–displacement behavior of irregularly shaped particles. Instead, its purpose is to provide an analogy to the linear contact model widely employed in DEM.

The results of the Hertzian contact case are present in Fig. 11. In this case, the force–displacement profile exhibits a smoother increasing rate compared to the results of the linear contact potential. The results from ten different simulations display some variation but are generally

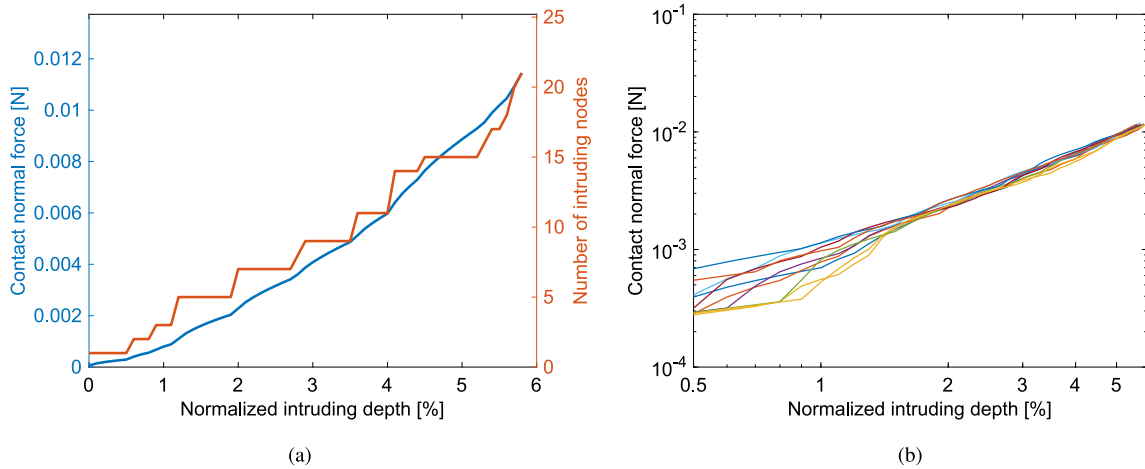


Fig. 11. Force–displacement profiles of the irregularly shaped and Hertzian case of contact test (a) and the results of ten different random sets of surface nodes (b).

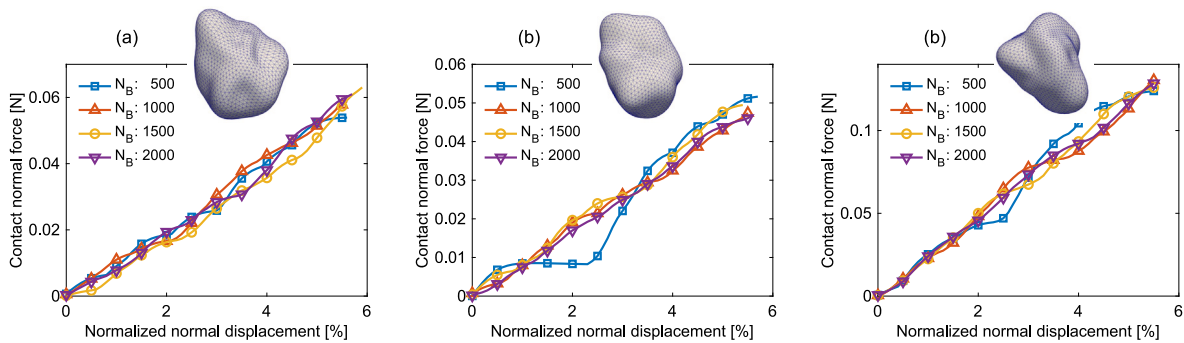


Fig. 12. Force–displacement profiles for irregularly shaped particles with varying numbers of surface nodes under the linear contact condition, where (a), (b), and (c) represent the results of three different particles.

in good agreement. The force–displacement profiles are best fitted by a power function, with an exponent of about 1.55 for the irregularly shaped case. This suggests that the proposed three-halves-power contact potential adeptly reproduces the characteristic features of the Hertzian contact, even in the context of irregularly shaped particles.

As for irregularly shaped particles, the number of surface nodes required for a converged force–displacement profile will be influenced by the complexity of the particle shape. To further investigate this, additional contact tests were conducted with several other irregularly shaped particles. Fig. 12 presents the force–displacement profiles for irregularly shaped particles under linear contact conditions, while Fig. 13 shows the profiles under Hertzian contact conditions. The linear contact force exhibits a relatively consistent trend across different surface node numbers, with slight variations in the force–displacement profiles observed as the number of surface nodes increases. This suggests that while the linear contact case shows some sensitivity to node density, increasing the number of surface nodes can improve accuracy. Conversely, the Hertzian contact profiles demonstrate similar consistency across different surface node numbers, indicating that the Hertzian contact case is less sensitive to changes in node density compared to the linear contact case. These results suggest that for both linear and Hertzian contact scenarios, a surface node number of around 1000 provides an optimal balance between computational efficiency and accuracy for the irregularly shaped particles.

5.1.3. Effect of surface curvature

To investigate the influence of particle surface curvature on contact behavior, 100 irregularly shaped particle contact tests with different particle orientations are conducted. In each trial, two particles were assigned random orientations, resulting in different surface curvatures at

the contact position. The results of 100 contact test trials are presented in Fig. 14. The curvature radius is defined as the inverse of the average of the major and minor surface curvatures of all intruding surface nodes. The equivalent contact normal stiffness and Young’s modulus are determined by regression analysis of the force–displacement profiles.

For the linear contact case, the equivalent contact normal stiffness ranges from 0.5 N/m to 3.5 N/m, with a reasonable deviation from the value of 1.57 N/m for the two spheres, as shown in Fig. 5. In addition, a modest positive correlation with the radius of curvature is observed, consistent with the relation (11). For the Hertzian contact case, the equivalent Young’s modulus falls in the range of 0.5 Pa to 2.5 Pa, fluctuating around the value of 1.53 Pa (see Fig. 9). Interestingly, the equivalent Young’s modulus does not exhibit a significant correlation with the radius of curvature, aligning with the implication of Eq. (18).

5.1.4. Effect of size ratio

Moreover, contact tests involving two particles of differing sizes were conducted to explore the impact of size ratio on their contact behavior based on the proposed contact potential models. Following a similar setup to the spherical case, one particle was maintained at a constant size of 1 m, while the size of the other varied from 0.1 m to 1.0 m. Both linear and Hertzian scenarios were examined, and the equivalent normal stiffness and Young’s modulus were determined based on simulated force–displacement profiles. For comparison, analytical equivalents of the normal stiffness and Young’s modulus were calculated from Eqs. (11) and (18). Fig. 15 illustrates the comparison between simulated and analytical results, demonstrating a high degree of agreement. Overall, the above results demonstrate the reasonable performance of the developed relationships between the contact parameters in SDF-DEM and those of conventional linear and Hertzian contact models.

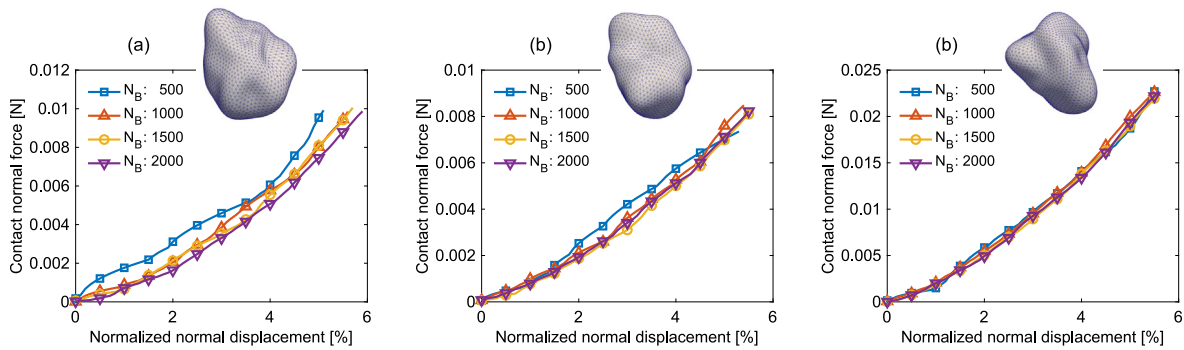


Fig. 13. Force-displacement profiles for irregularly shaped particles with varying numbers of surface nodes under the Hertzian contact condition, where (a), (b), and (c) represent the results of three different particles.

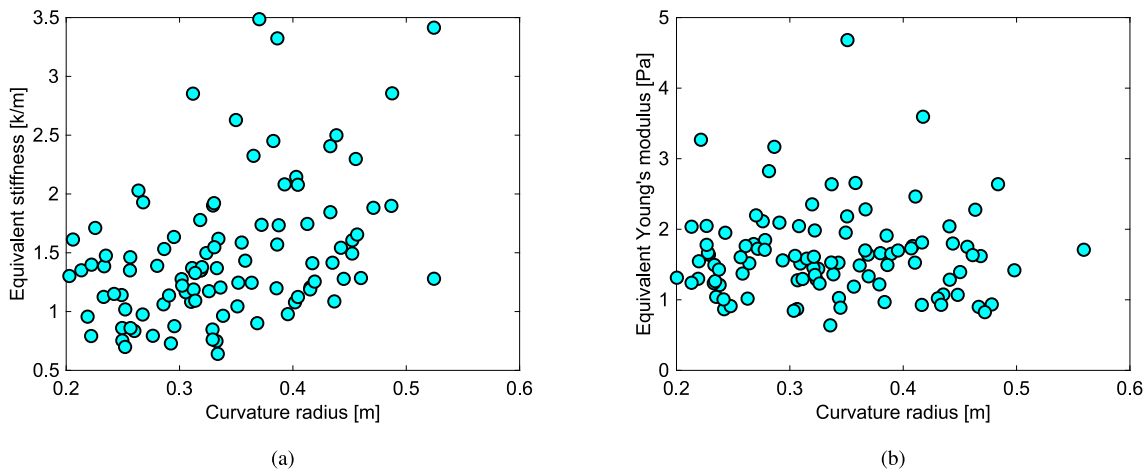


Fig. 14. Effect of surface curvature on the equivalent contact stiffness modeled by SDF-DEM for (a) linear contact case and (b) Hertzian contact case.

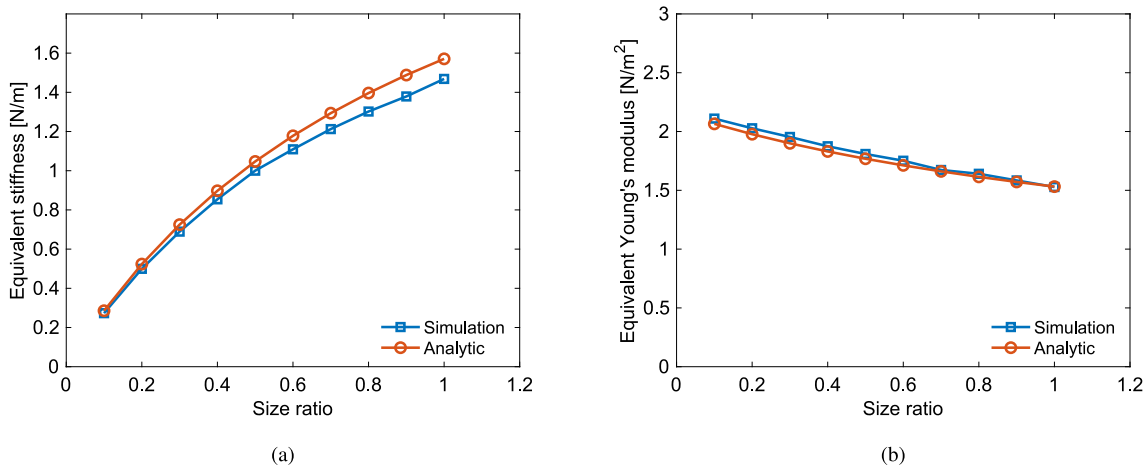


Fig. 15. Effect of particle size ratio on the equivalent contact stiffness modeled by SDF-DEM for (a) linear contact case and (b) Hertzian contact case.

It is noted that, in this work, the proposed linear and Hertzian contact potential formulations within SDF-DEM are compared with the theoretical linear and Hertzian contact behavior but have not yet been compared with experimental data. In reality, the contact between two particles can be very complex under the influence of many factors, such as particle shape, material type, contact history, etc. The widely used linear and Hertzian contact models in DEM are originally developed based on spheres and then extended to irregular shapes with reasonable assumptions. As a first attempt, this work aims to establish a link between the contact behavior of SDF-DEM and conventional DEM. The

comparison with experimental data, typically considering the effects of particle shape and material type, will be explored in the future. It is also worthwhile noting that the node-to-surface contact algorithm is adopted by SDF-DEM in a manner similar to the finite element analysis. Thus, the SDF-DEM framework is of good flexibility and accuracy to be extended to consider the effects of particle shape and material type.

5.1.5. Contact shear behavior

The shear contact force in this model is not derived from the contact potential formulations but is instead determined using the classical

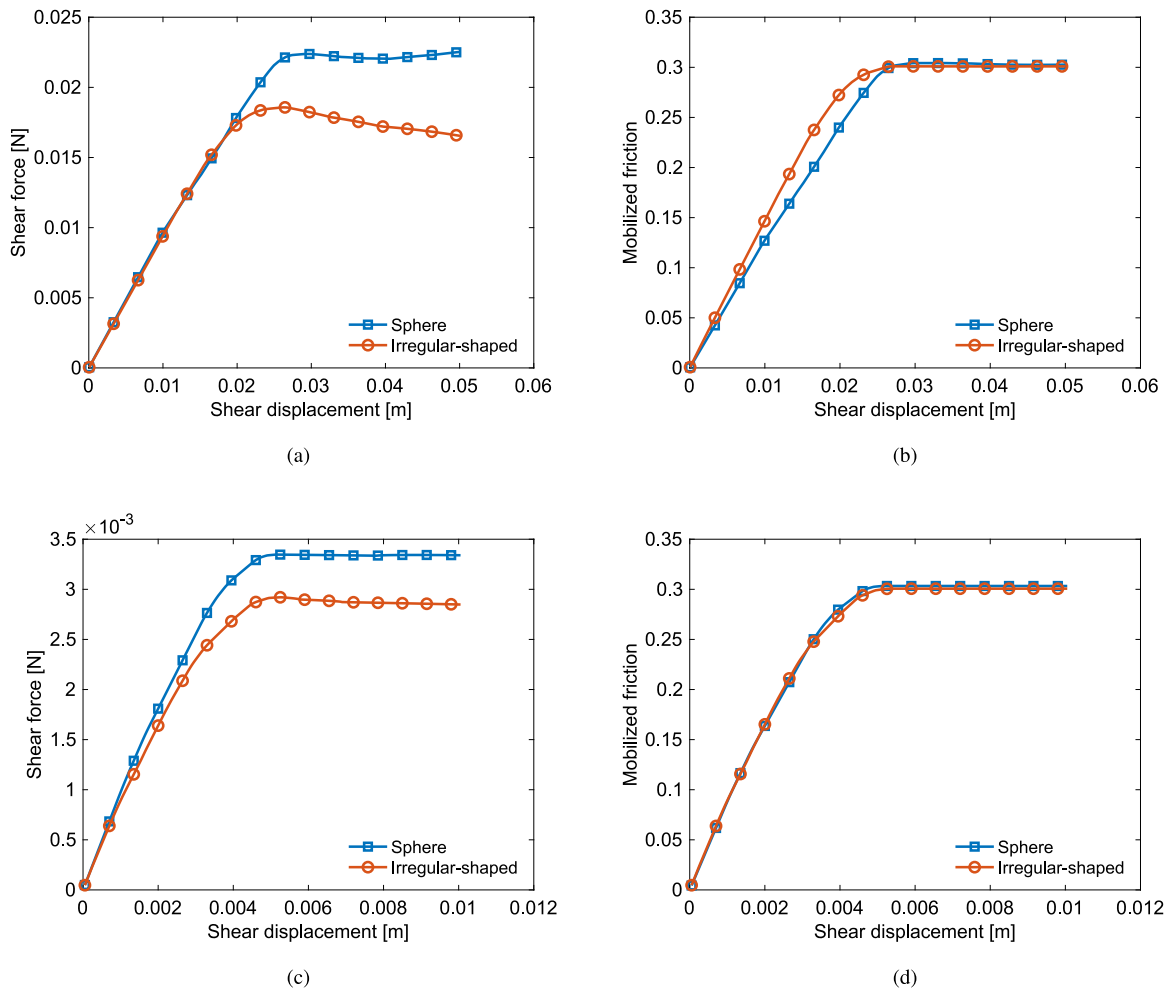


Fig. 16. Evolution of (a) contact shear force and (b) mobilized friction for the linear contact case, and (c) contact shear force and (d) mobilized friction of the Hertzian contact case with increasing shear displacements.

linear contact model in conjunction with Coulomb's law of friction. To investigate the shear contact behavior, a shear contact test is conducted with a setup similar to that shown in Fig. 4. In this test, Particle *A* is anchored at the origin, while Particle *B* is positioned above Particle *A*, with their centroids aligned along the *z* axis. Particle *B* is first moved downwards to create an initial overlap of about 5% of the particle size, and then moved in the positive *x* direction to generate a shear force. Without loss of generality, the contact shear stiffness is set to 1 N/m, and the contact friction coefficient is set to 0.3. The evolution of shear contact force and mobilized friction with increasing shear displacement for both linear and Hertzian contact cases is plotted in Fig. 16. The mobilized contact friction is computed as the current contact shear force divided by the contact normal force. The results indicate that the shear force exhibits a reasonable linear relationship with the shear displacement during the elastic stage, before plateauing at the ultimate shear force, as governed by Coulomb's law of friction. A slight difference in shear behavior is observed between the spherical and irregular-shaped particle cases, primarily due to the effect of particle morphology. Overall, the results demonstrate the effectiveness of the adopted linear shear contact model and Coulomb's law of friction.

5.2. Energy conservation test

To assess the energy-conserving properties of the proposed contact theory, a DEM simulation is performed involving the free fall of two particles and their collision with a ground boundary. The setup, as depicted in Fig. 17, consists of two particles placed inside a cubic box

of unit dimensions. The initial separation between the two particles is approximately 0.5 m. Each particle has an equivalent size of 0.1 m, a density of 2650 kg/m³, and is subjected to the gravitational acceleration of 9.81 m/s². The model parameters include a normal stiffness parameter k_i set to be 1.0×10^7 N/m², with no damping or contact friction applied. The simulation time duration is 3.0 s, utilizing a fixed timestep of 1.0×10^{-4} s. Throughout the simulation, the translational, rotational, potential and total energies of the two particles are recorded for analysis.

The results of the energy evolution for the spherical and irregularly shaped cases, considering both linear and Hertzian contacts, are presented in Fig. 18. The reference for the gravitational potential energy is set at $z = 0$ m. In all figures, the sharp troughs in the gravitational potential energy correspond to collision events between particles and the ground boundary. The rotational energy remains close to zero throughout the simulation for the spherical case, while a significant variation is observed for the irregularly shaped particles. This is expected since contact normal forces generally do not pass through the centroid of non-spherical particles, inducing rotation. Moreover, it is important to note that, even for spherical particles based on the proposed contact theory, the contact normal force might not pass through the particle centroid due to the possible unsymmetrical distribution of surface nodes within the contact area. Although the deviation in the orientation of the contact normal is generally small and not evident in the simulation of spherical particles, the total energy of the two particles is well conserved in both cases.

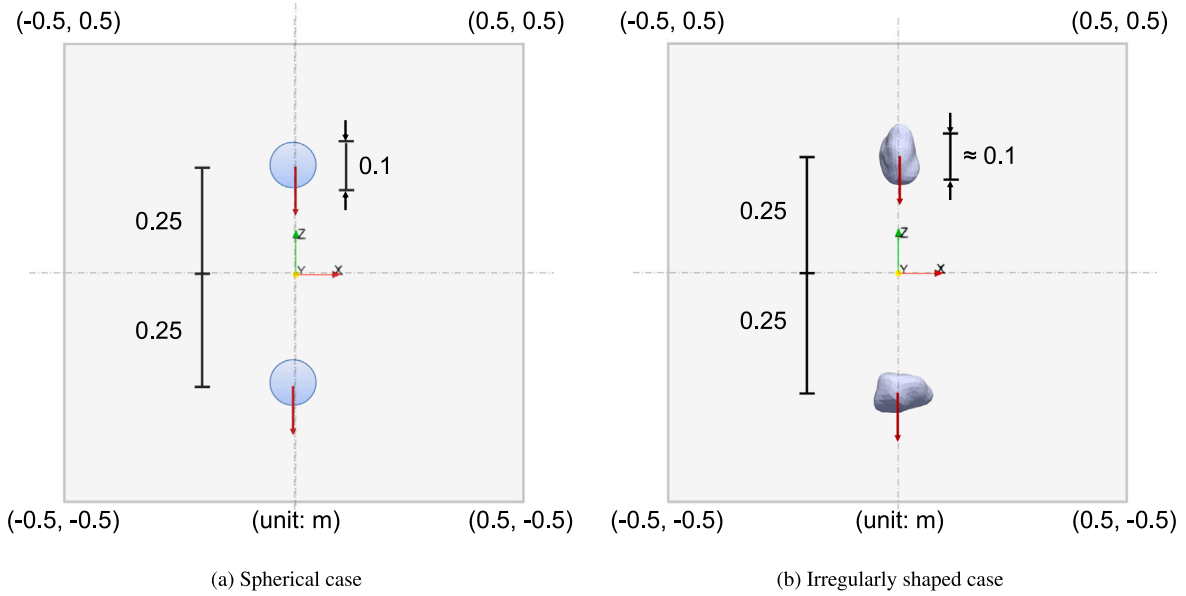


Fig. 17. Sketch of the setup of the energy conservation test.

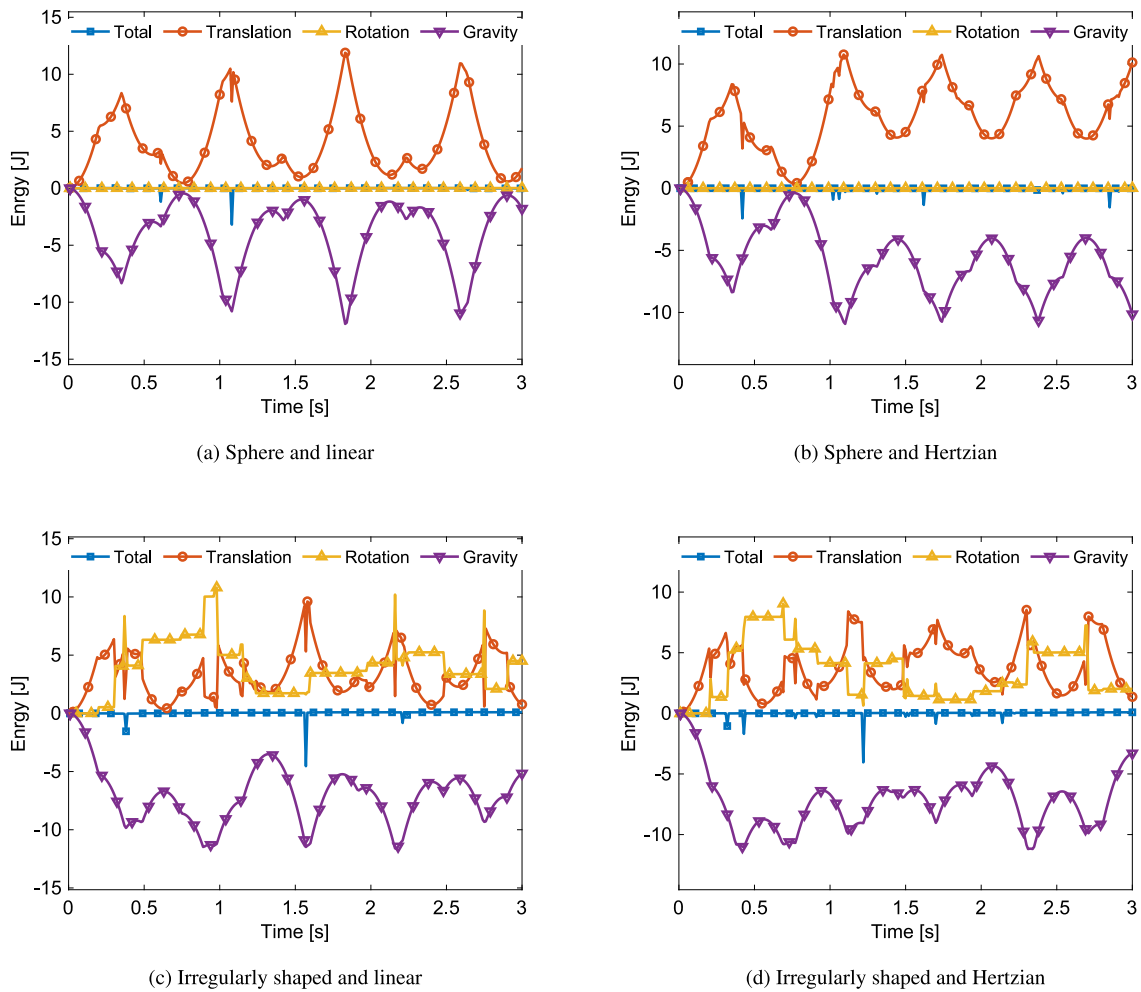


Fig. 18. Evolution of translational, rotational and gravitational potential and total energies of the two particles during the energy conservation test: (a) sphere and linear case, (b) sphere and Hertzian case, (c) irregularly shaped and linear case, and (d) irregularly shaped and Hertzian case.

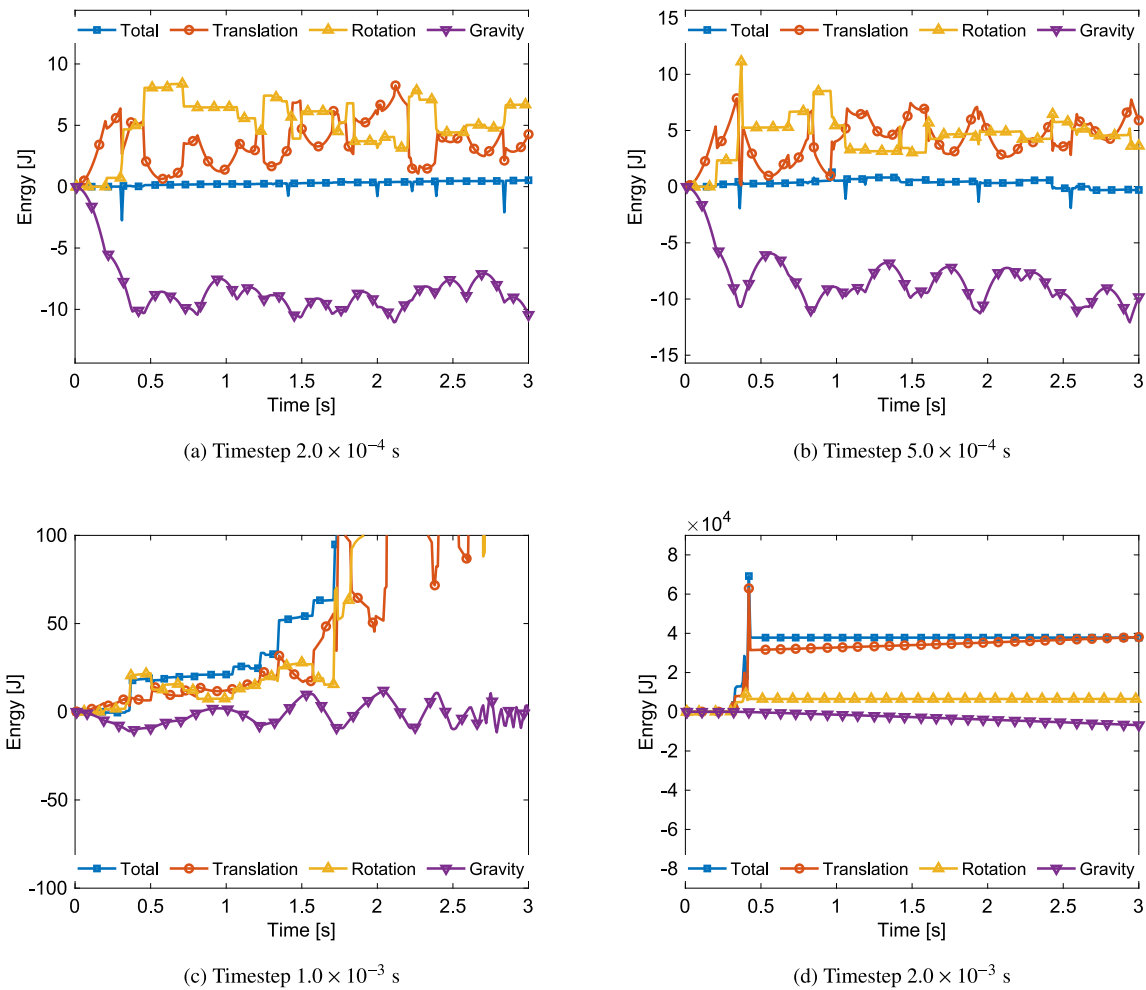


Fig. 19. Evolution of translational, rotational and gravitational potential and total energies of the energy conservation test for the case of irregularly shaped particle and linear contact: (a) timestep 2.0×10^{-4} s, (b) timestep 5.0×10^{-4} s, (c) timestep 1.0×10^{-3} s, and (d) timestep 2.0×10^{-3} s.

5.3. Critical timestep test

To explore the critical timestep issue, the previous energy-conserving test is conducted with different timestep values for the linear contact case. According to Eq. (12), the critical timestep is estimated to be approximately 9.4×10^{-4} s, for a particle mass m of about 1.4 kg and an equivalent translational contact normal stiffness k_n of 1.6×10^6 N/m. Fig. 19 displays the energy evolution of the irregularly shaped case at different timesteps. For a timestep of 5.0×10^{-4} s, small energy variations are observed after each collision. As the timestep increases to 1.0×10^{-3} s, the total energy notably increases after each collision, and the results deteriorate further with a timestep of 2.0×10^{-3} s. The sensitivity of the results to timestep variations agrees reasonably well with the estimated critical timestep 9.4×10^{-4} s, indicating the compatibility between the proposed linear contact potential-based contact behavior and the conventional critical timestep analysis.

In the Hertzian contact case, by substituting the model parameters into Eq. (20) and assuming the largest permissible penetration depth δ_n equal to 5% of the particle size, the largest transient translational contact normal stiffness k_n is calculated to be approximately 2.3×10^5 N/m. Utilizing Eq. (12), the estimated critical timestep is approximately 2.5×10^{-3} s. In the energy conservation test, specifically for irregularly shaped particles, Fig. 20 illustrates the energy evolution with different timesteps. When the timestep is 1.0×10^{-3} s or less, the total energy is well conserved with only small variations. Upon increasing the timestep to 2.0×10^{-3} s, notable variations in the total

energy are observed after each collision. Finally, when the timestep is increased to 5.0×10^{-3} s, the simulation becomes unrealistic, with infinite energy gain after collisions. Overall, the results demonstrate the good consistency between the critical timesteps for contact modeling based on the proposed contact potential models within SDF-DEM and the conventional contact models.

To further analyze the impact of timestep on the stability and accuracy of simulations under varying conditions, we conducted three energy tests involving multiple irregularly shaped particles with different timestep and friction settings. Fig. 21 presents snapshots of the particles at initial packing and after specific simulation periods. In Case II, with a timestep of 1.0×10^{-3} s and no friction (Fig. 21(c)), the particles experienced an early explosion at 0.02 s, resulting in extremely large spurious velocities. By using a computationally stable timestep of 1.0×10^{-4} s, the particles maintained conserved total energy in the frictionless case, as shown in Fig. 21(b). Additionally, when the coefficient of friction was set to 0.3, the particles essentially reached a quasi-static stage, as depicted in Fig. 21(d). These observations are further corroborated by the quantitative energy analysis results illustrated in Fig. 22, which detail the evolution of total, translational, rotational, and gravitational energies under different conditions.

5.4. Multiple-sphere shearing simulation

The multiple-sphere shearing test involves 1250 spherical particles of size 0.005 m. Illustrated in Fig. 23, the test consists of three main steps: packing, equilibrium, and shearing. During the packing step, ten

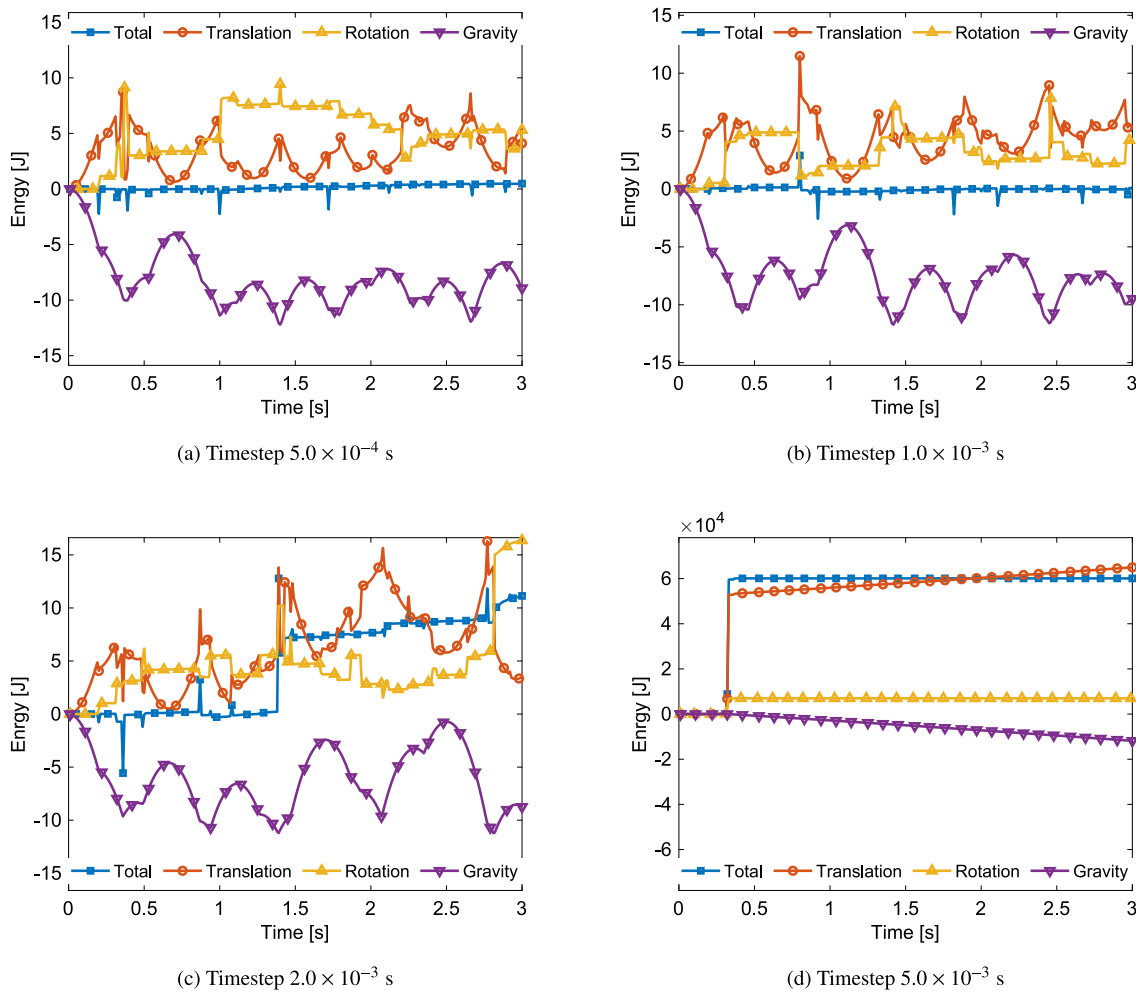


Fig. 20. Evolution of total, translational, rotational and gravitational energies of the energy conservation test for the case of irregularly shaped particle and Hertzian contact: (a) timestep 5.0×10^{-4} s, (b) timestep 1.0×10^{-3} s, (c) timestep 2.0×10^{-3} s, and (d) timestep 5.0×10^{-3} s.

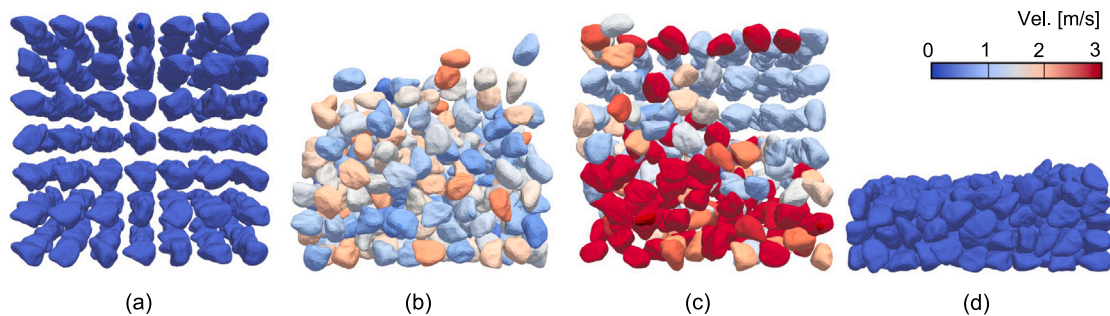


Fig. 21. Illustration of the energy test of multiple irregularly shaped particles with different timestep and friction conditions: (a) initial packing, (b) after 3.0 s for Case I with a timestep of 1.0×10^{-4} s and no friction, (c) after 0.02 s for Case II with a timestep of 1.0×10^{-3} s and no friction, and (d) after 3.0 s for Case III with a timestep 1.0×10^{-4} s and a friction of 0.3.

packs of 125 particles are successively injected into the upper part of the box container with a base of 0.04–0.04 m. The particles are allowed to settle under gravity, and each injection is made at a time interval of 0.1 s to ensure that particles from the injection region before the next insertion. After ten injections, the particles undergo an equilibrium period of 0.5 s. Moving on to the shearing step, the particles are initially compressed with an isotropic pressure of 200 kPa and then subjected to shear by lowering the top wall at a speed of 0.002 m/s while maintaining a lateral confining pressure of 200 kPa through servo control (Abbas et al., 2005; Faramarzi et al., 2020). The

shearing process lasts for 10 s, resulting in a final axial strain of about 25%.

In this example, the Hertzian contact potential is employed for SDF-DEM, while the conventional Hertzian contact model is used for the conventional DEM. The simple linear frictional behavior is adopted in both SDF-DEM and conventional DEM. For SDF-DEM, the model parameters are set as follows: the normal stiffness parameter k_i is 8.5×10^7 N/m², the shear stiffness k_s is 1.0×10^5 N/m, and the contact friction μ is 0.3. Notably, the chosen normal stiffness parameter k_i equates to an equivalent conventional normal stiffness of 1.0×10^5 N/m at a contact overlap equal of 0.05% of the particle size. It is highlighted that, in this

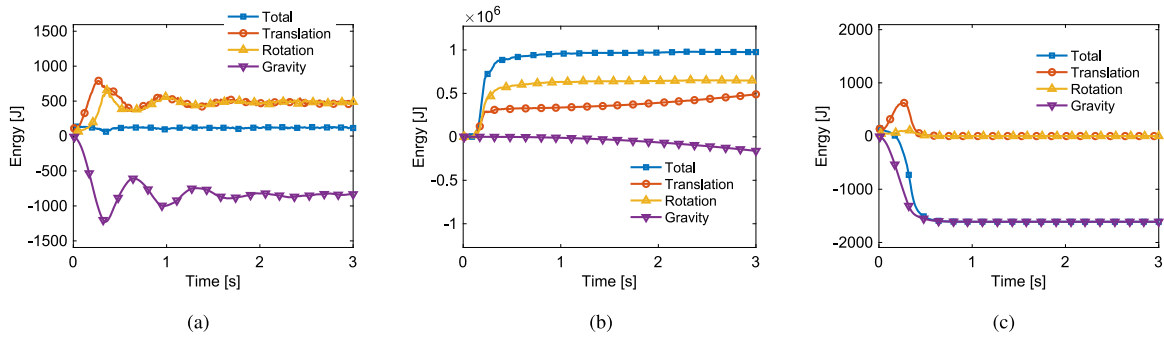


Fig. 22. Evolution of the total, translational, rotational and gravitational energies of the multiple irregularly shaped particles in the energy test with different timestep and friction conditions: (a) Case I with a timestep of 1.0×10^{-4} s and no friction, (b) Case II with a timestep of 1.0×10^{-3} s and no friction, and (c) Case III with a timestep 1.0×10^{-4} s and a friction of 0.3.

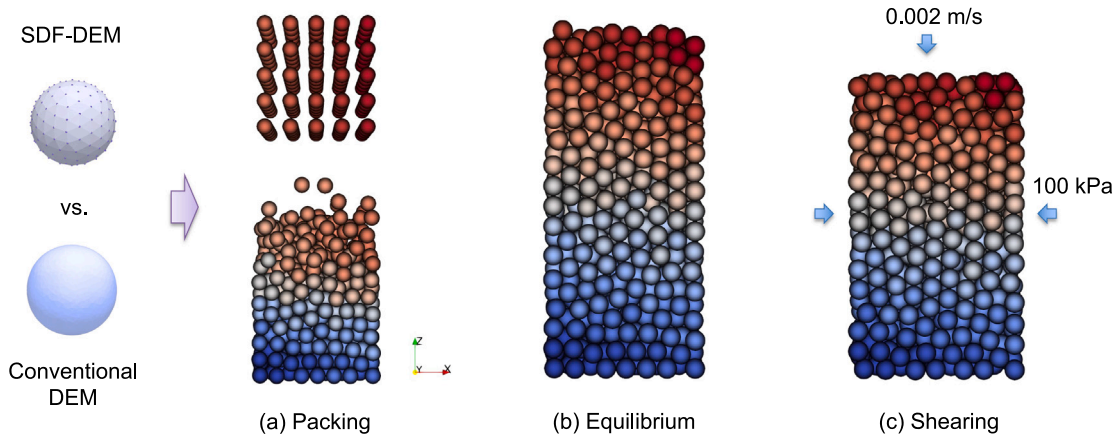


Fig. 23. Illustration of the three main steps, namely (a) packing, (b) equilibrium, and (c) shearing, of the triaxial compression test.

work, each intruding node carries a contact friction force, with the total contact frictional force between two particles calculated as the average of all intruding nodes. Consequently, SDF-DEM and the conventional DEM exhibit equivalent contact friction behavior for the same shear stiffness. The particles are discretized with surface nodes. Accordingly, for the conventional DEM, the equivalent Young's modulus E^* is 1.35×10^8 N/m², the shear stiffness k_t is 1.0×10^5 N/m, and the coefficient of contact friction μ is 0.3. In both cases, the particle density is 2.65×10^5 kg/m³, artificially increased by two orders of magnitude from the conventional density of sand particles to accommodate a timestep of 1.0×10^{-4} s. The classical velocity-based damping force and moment (Andrade et al., 2012; Lim and Andrade, 2014) are considered with a damping coefficient of 3.0.

The results of particle kinetic energy, stress-strain relation, coordination number, and contact force distributions are presented to gain insights into the accuracy and numerical stability of the proposed Hertzian contact potential within the SDF-DEM framework. Fig. 24 shows the evolution of average particle velocity during the packing and equilibrium processes. During the packing process, particles are gradually injected from a certain height, resulting in a slow decrease of the average particle velocity. During the equilibrium process, the particle average velocity decreases rapidly to less than 1.0 mm/s. These results indicate that the proposed framework exhibits good numerical stability. Fig. 25 plots the results of stress-strain evolution during the shearing process. The deviatoric stress ratio initially increases rapidly and then decreases gradually. Similarly, the volumetric strain first increases slightly, indicating a contraction process, and then decreases, indicating a dilation process. An interesting observation is that the SDF-DEM appears to capture the critical state condition better than the conventional DEM, as evidenced by a more leveled stress-strain

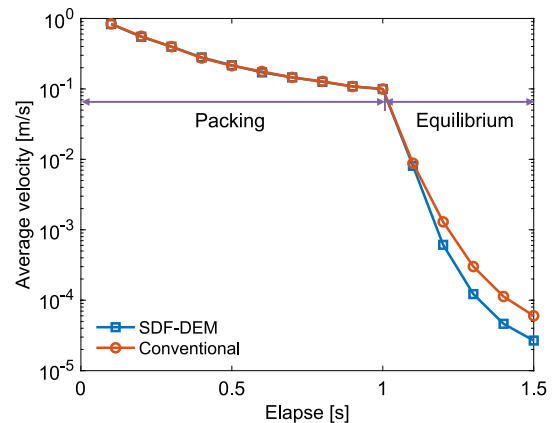


Fig. 24. Evolution of particle average velocity during the packing and equilibrium processes for the spherical case.

evolution during the critical state. However, with the proposed linear and three-halves formulations of contact potential, the SDF-DEM is expected to be capable of theoretically reproducing both the linear and Hertzian contacts as modeled in the conventional DEM. Therefore, for spherical particles, the triaxial compression results of the SDF-DEM should closely align with those of the conventional DEM. Based on the current results and our previous work (Lai et al., 2022), we suspect that the observed differences in the critical state condition between the SDF-DEM and the conventional DEM may primarily be due to the effects of packing randomness.

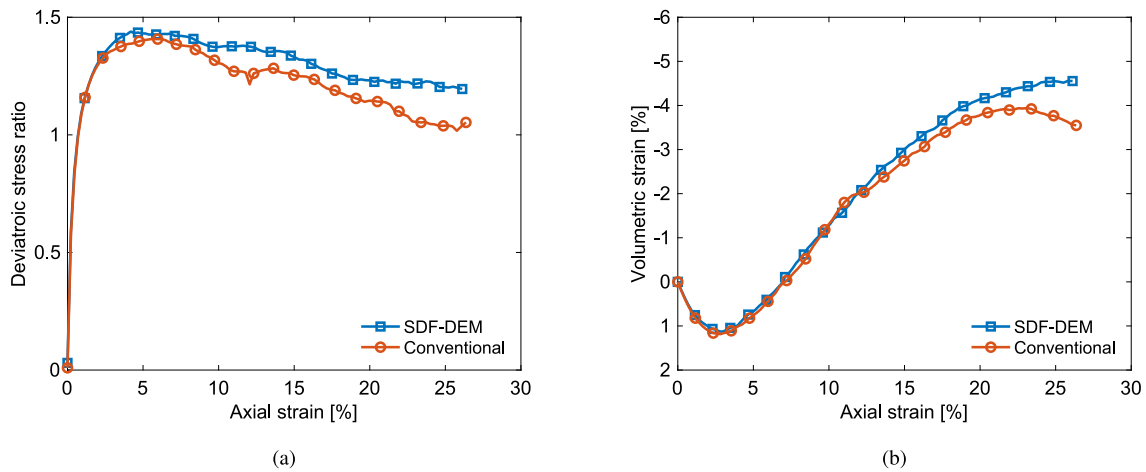


Fig. 25. Evolution of (a) deviatoric stress ratio and (b) volumetric strain with increasing axial strain during the triaxial shearing in the spherical case.

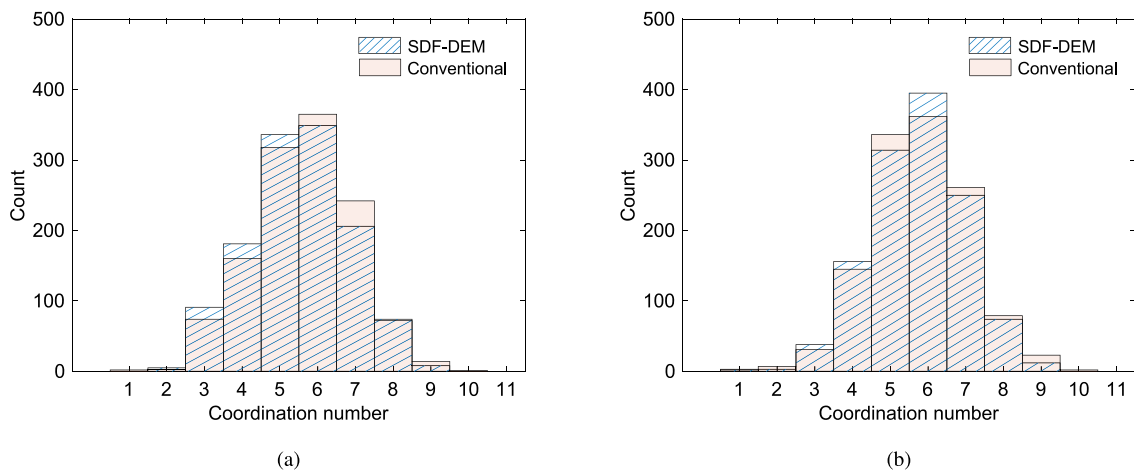


Fig. 26. Coordination number distribution of the particles: (a) after equilibrium and (b) at 5% axial strain during shearing in the spherical case.

Fig. 26 compares the coordination number of the particles after equilibrium and during shearing. For both SDF-DEM and conventional DEM, the dominant coordination number is of 6, and the coordination number hardly varies during the shearing process. Fig. 27 plots the distribution of the contact forces of the particles at the axial strain of 5%. The contact normal force is mainly concentrated within three times the average contact normal force, with the average contact normal force being about 6.8 N and 6.7 N for the SDF-DEM and conventional DEM cases, respectively. The contact frictional force is mainly within one time of the average contact normal force. Using Eq. (17), the contact overlap is calculated to be approximately 2.1% of the particle size for the average contact normal force of 6.8 N and 4.4% for three times the average contact normal force.

Referring to the results presented in Fig. 9(a), there are about 13 intruding nodes for a contact overlap of 2.1% and 27 intruding nodes for an overlap of 4.4%. In this context, the node-based contact friction model is likely have an overall contact tangential stiffness that is approximately 20 times that of the contact tangential stiffness of the conventional linear contact model, if the total contact frictional force is not taken as the average. Nonetheless, the exact contact tangential stiffness depends on factors such as contact normal force, contact history, and contact surface complexity, and it varies among individual particles. The node-based contact frictional model offers the advantage of providing the contact area-related frictional behavior and can replicate the rotational resistance of the contact due

to friction. Overall, all results of SDF-DEM and conventional DEM are in reasonable agreement, verifying the good accuracy of the SDF-DEM and the proposed contact potential model.

In practice, there exists two challenges in applying SDF-DEM to irregularly shaped particles. The first is finding the right balance between accuracy and computational cost when selecting an appropriate number of surface nodes. The second challenge is the computational expense. While SDF-DEM has been shown to be more accurate and computationally efficient than the clump-DEM approach, it remains significantly more expensive, being approximately 100 times slower than conventional sphere-based DEM. Future research could focus on exploring GPU parallel acceleration techniques and machine learning-based surrogate algorithms to enhance the efficiency of contact detection and resolution. By employing the SDF for particle shape description and the node-to-surface algorithm for contact detection and resolution, SDF-DEM eliminates the need for an explicit mesh for the particles. Instead, particles are discretized with surface nodes, where contacts are defined. The effectiveness of SDF-DEM in modeling irregularly shaped particles has been validated in previous works (Lai et al., 2022, 2023; Huang et al., 2023) through various examples, including triaxial compression, column collapse, and mudflow simulations. This work aims to unify the contact in the SDF-based and the conventional DEM. For this purpose, spherical particles with analytical contact behavior are used for the verification in this section.

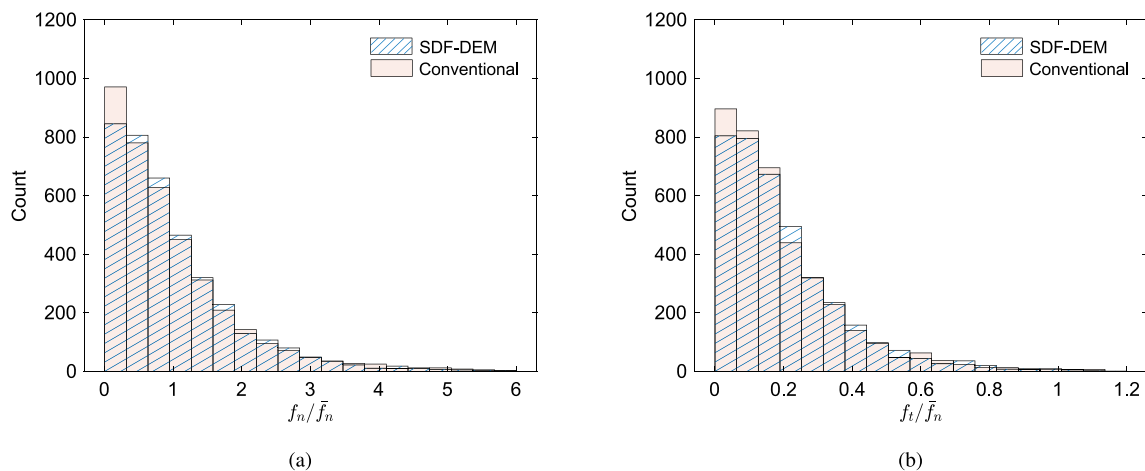


Fig. 27. Distribution of particle contact forces at 5% axial strain during shearing in the spherical case: (a) contact normal force, and (b) contact frictional force. Both the contact normal (f_n) and shear (f_t) forces are normalized by the average contact normal force (\bar{f}_n).

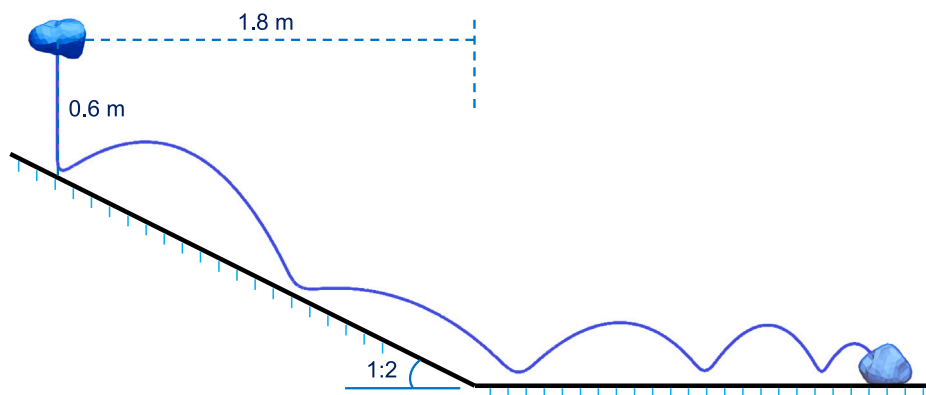


Fig. 28. Sketch of the irregularly shaped particle rockfall simulation.

5.5. Irregularly shaped particle rockfall simulation

In the rockfall simulation, an irregularly shaped particle is positioned 1.8 m horizontally away from the foot of a slope measuring 0.6 m in height, with an inclination of 1:2 (see Fig. 28). The particle has an equivalent diameter of 0.2 m and a density of 2650 kg/m^3 . Linear contact modeling is employed for this example, considering two cases of equivalent contact stiffnesses, namely $1.0 \times 10^4 \text{ N/m}$ and $1.0 \times 10^5 \text{ N/m}$, respectively. The trajectory of the particle in the rockfall simulation is notably sensitive to the contact stiffness, offering same insight into the validity and robustness of the developed contact models. Moreover, to explore the discretization issue of SDF-DEM, two scenarios of surface node discretization are investigated: one with 1000 nodes and the other with 2000 nodes. A contact friction coefficient of 0.3 and viscous damping coefficient of 1.0 are applied. The timestep remains fixed at $1.0 \times 10^{-4} \text{ s}$. The simulation runs for 5.0 s, during which the particle eventually comes to rest, reaching a near-steady state. Each case includes 10 trials with different random configurations of surface nodes to evaluate the effects of randomness.

The particle trajectories throughout the rockfall process for all scenarios are plotted in Fig. 29. Notably, particles subjected to a higher contact stiffness (i.e., $1.0 \times 10^5 \text{ N/m}$) exhibit greater translational distances compared to those with a lower contact stiffness (i.e., $1.0 \times 10^4 \text{ N/m}$). This disparity can be attributed to the shorter duration of contact collisions associated with the higher contact stiffness, resulting in less energy dissipation due to contact friction. For cases with an identical contact stiffness, the results obtained with 1000 and 2000

surface nodes demonstrate considerable consistency. The final positions of the particles, illustrated in Fig. 30, reveal intriguing patterns. In the scenario featuring a contact stiffness of $1.0 \times 10^4 \text{ N/m}$, the final positions cluster within a confined region. Conversely, as the contact stiffness increases, the final positions exhibit greater variability, and the variance would be reduced by increasing the number of surface nodes. It is imperative to acknowledge that the particle trajectory and final position in the rockfall simulations are highly sensitive to the behavior of each contact. Even minor fluctuations in contact forces can yield significant alterations in particle velocity and subsequent orientation at the next contact instance following a given falling duration. Consequently, these deviations amplify over time, resulting in pronounced differences in the final particle positions. In summary, the results from the four different cases elucidate the anticipated trends and underline the validity and robustness of the developed contact potential model within SDF-DEM.

6. Discussion

It is noted that the clump (Das, 2007; Wu et al., 2021) and LS approaches (Kawamoto et al., 2016) are two widely adopted methods for modeling irregularly shaped particles in DEM. Similar to the classical DEM originally proposed by Cundall and Strack (1979), these two approaches, along with SDF-DEM, follow the same governing equations and computational steps: (1) resolving contact features, (2) evaluating contact behavior, (3) calculating particle motion, and (4) updating the particle geometric description. The primary differences among

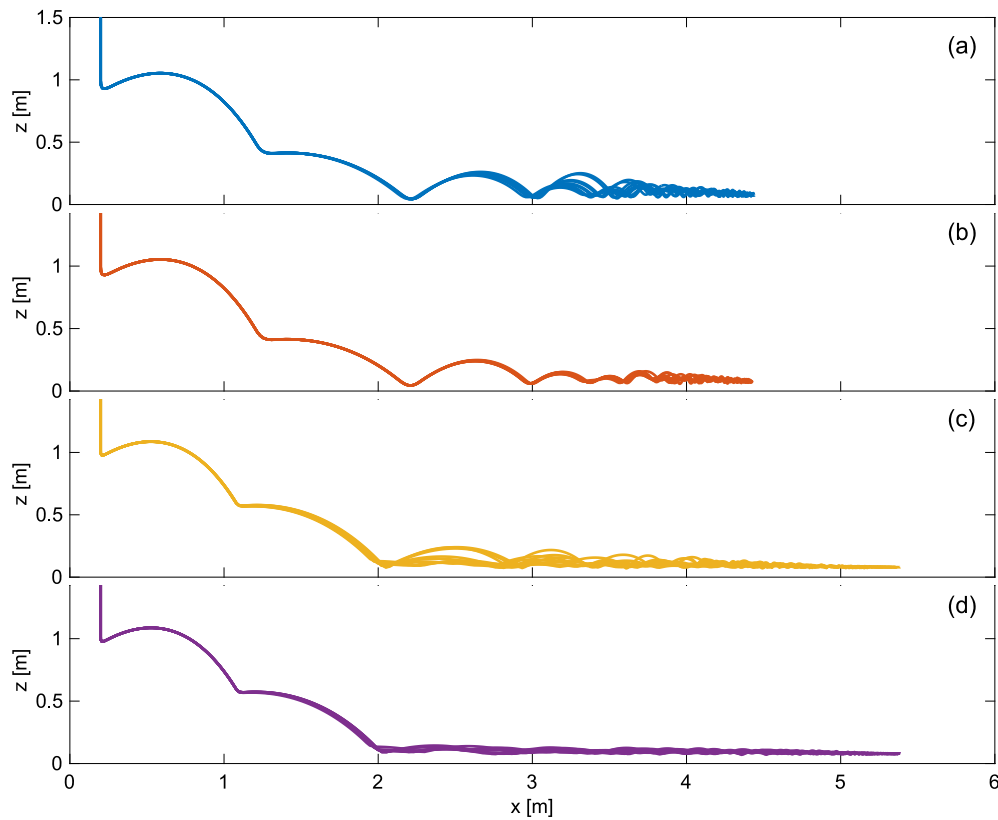


Fig. 29. Particle trajectories in the rockfall process for scenarios of (a) contact stiffness 1.0×10^4 N/m², surface nodes 1000, (b) contact stiffness 1.0×10^4 N/m², surface nodes 2000, (c) contact stiffness 1.0×10^5 N/m², surface nodes 1000, and (d) contact stiffness 1.0×10^5 N/m², surface nodes 2000.

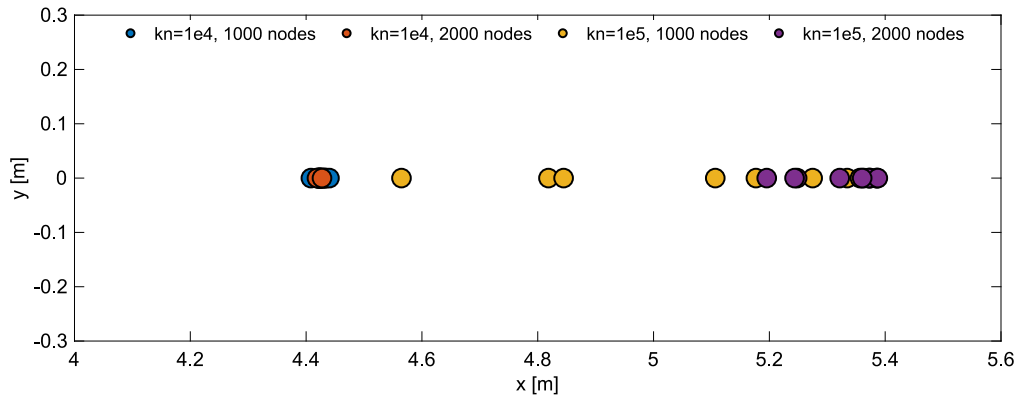


Fig. 30. Final positions of the rockfall particles at the end of simulation for different cases and random trials.

them lie in the particle shape descriptions and contact algorithms. In the clump approach, an irregularly shaped particle is represented by a set of clumped spheres, with contacts defined between each pair of colliding sub-spheres. For the level set-DEM, it utilizes a node-to-surface algorithm to manage contacts, similar to SDF-DEM. The SDF-DEM can be considered a superset of LS-DEM, employing a broad-sense signed distance function to describe particle shapes. Contact behavior in SDF-DEM is derived from a contact potential function in an energy-conserving manner. The SDF-DEM converges to the LS-DEM under two specific conditions. First, a discrete level set is used for the signed distance function; and second, the node-wise contact potential is considered as half the square of the signed distance multiplied by a stiffness parameter k (i.e., $F(d_i(\vec{x}, \vec{\theta})) = 0.5kd_i^2$), analogous to the elastic potential of a linear spring. The node-wise contact force is thus computed as $kd_i\vec{n}$, where \vec{n} represents the gradient of the signed distance, i.e., the normal of the level set contour.

It is also noted that the SDF-DEM could be approximately 100 times computationally more expensive than the classical DEM for spheres and 5~10 times than the GJK-DEM (Wachs et al., 2012) for convex particles. Since the framework of SDF-DEM is similar to that of the classical DEM, conventional acceleration strategies, such as the linked-list algorithm (Muth et al., 2007) for the coarse-phase contact detection and paralleled updating of particle motion, can be directly applied to SDF-DEM. These strategies have been implemented in the CPU (central processing unit) version of SDF-DEM, and our code now supports hybrid parallel computation using OpenMP (open multi-processing) and MPI (message passing interface). Additionally, our colleagues have recently developed a GPU (graphics processing unit) version of SDF-DEM, incorporating a novel ray-tracing approach to achieve ultra-high efficiency for large-scale particle simulations (Zhao and Zhao, 2023). This GPU implementation leverages not only the CUDA (compute unified

device architecture) cores but also the ray-tracing cores to efficiently query the SDF for the surface nodes of particles, thereby fully unleashing the computing power of the GPU. Nonetheless, further exploration on parallelization strategies and GPU acceleration is worthwhile to benefit users applying this method to large-scale simulations.

Besides mapping SDF-DEM contact behavior to DEM contact models, mapping the SDF-DEM to physical models offers practical benefits. As this is an initial effort to develop a new method, our primary focus is on developing the methodology and demonstrating its potential for irregular-shaped particle mechanics. By mapping SDF-DEM to traditional DEM with parameter continuity, we validate the new method against established benchmarks and datasets, facilitating quicker adoption and understanding of the new approach. While DEM contact models require parameter fitting, the parameters used are well documented and have been successfully applied to various practical problems. Mapping SDF-DEM to DEM models helps in understanding how new parameters relate to traditional ones, easing the transition and ensuring continuity in parameterization. This consistency in simulations allows for direct comparison of results between SDF-DEM and traditional DEM. Additionally, it is worth noting that the potential-based contact theory adopted in SDF-DEM provides a robust and flexible way to approach complex contact behavior by developing new formulations of contact potential. More choices in contact potential formulations and mapping with physical models will be explored in the future.

The exact contact behavior between two particles would be affected by the particle surface morphology. However, a closed-form analytical formulation of the contact behavior of generally irregular-shaped particles is not yet available in DEM. The framework proposed in this work takes significant steps to address these challenges. Specially, the surface curvature at the contact points, which is relevant to particle surface morphology, is accounted for in the developed formulations of contact potential. In addition, the scenario of multiple contacts is naturally considered due to the node-based definition of contact behavior. In this sense, the formulations are sufficiently general to accommodate arbitrary particle surface morphologies. The effect of particle surface morphology on the contact behavior is incorporated to a certain extent.

7. Summary

In this paper, we have developed two formulations of contact potential, namely a linear contact potential drawing an analogy to the linear contact model and a three-halves-power contact potential serving as an analogy to the Hertzian contact model for SDF-DEM (or LS-DEM). Through thorough investigations into the force–displacement profile, energy-conserving characteristics, and critical timestep issues, we have gained insights into the contact behavior governed by the proposed contact potential. Moreover, qualitative relationships between the model parameters of the proposed contact theory and conventional contact models have been established, enhancing the understanding and practicality of the SDF-DEM framework. The accuracy and numerical stability of the proposed contact potentials and SDF-DEM have been verified based on DEM simulation results of triaxial compression tests and rockfall tests on spherical and irregularly shaped particles. It should be noted that the proposed contact potentials are not intended to precisely reproduce the force–displacement profile of irregularly shaped particles; rather, they provide analogies to conventional contact models widely used in previous DEM studies in an energy-conserving sense. By establishing comprehensive relationships between the parameters of the proposed contact theory and those of conventional contact models, we have facilitated a seamless integration between SDF-DEM and the conventional DEM. These findings not only advance the understanding of the energy-conserving contact theory but also provide a robust framework for bridging the gap between SDF-DEM and the conventional DEM. It is noted that SDF-DEM also offers significant advantages for modeling deformable particles incorporating with numerical techniques such as the finite element method, material point

method and smooth particle hydrodynamics. By defining contact forces on surface nodes, distributing boundary forces for computing particle deformation becomes straightforward. Ongoing efforts are underway to extend SDF-DEM and associated contact models to further enhance the modeling accuracy and efficiency of deformable particles.

CRedit authorship contribution statement

Zhengshou Lai: Writing – original draft, Validation, Software, Methodology, Formal analysis. **Y.T. Feng:** Writing – review & editing, Methodology, Investigation. **Jidong Zhao:** Writing – review & editing, Resources, Project administration, Investigation. **Linchong Huang:** Writing – review & editing, Resources, Project administration.

Declaration of competing interest

The authors declare that they have no known competing financial interests or personal relationships that could have appeared to influence the work reported in this paper.

Data availability

Data will be made available on request.

Acknowledgments

This work was financially supported by the Shenzhen Science and Technology Project for Sustainable Development, China (KCXFZ202002 011008532), the Research Grants Council of Hong Kong (16203123), and the National Natural Science Foundation of China (12072217). The work is also partially supported by the Project of Hetao Shenzhen-Hong Kong Science and Technology Innovation Cooperation Zone, China (HZQB-KCZYB-2020083).

References

- Abbas, A., Masa, E., Papagiannakis, T., Shenoy, A., 2005. Modelling asphalt mastic stiffness using discrete element analysis and micromechanics-based models. *Int. J. Pavement Eng.* 6 (2), 137–146.
- Andrade, J.E., Lim, K.W., Avila, C.F., Vlahinić, I., 2012. Granular element method for computational particle mechanics. *Comput. Methods Appl. Mech. Eng.* 241, 262–274.
- Belytschko, T., Yen, H., Mullen, R., 1979. Mixed methods for time integration. *Comput. Methods Appl. Mech. Eng.* 17, 259–275.
- Cho, G.C., Dodds, J., Santamarina, J.C., 2006. Particle shape effects on packing density, stiffness, and strength: natural and crushed sands. *J. Geotech. Geoenviron. Eng.* 132 (5), 591–602.
- Coetzee, C.J., 2017. Calibration of the discrete element method. *Powder Technol.* 310, 104–142.
- Cundall, P.A., Strack, O.D.L., 1979. A discrete numerical model for granular assemblies. *Géotechnique* 29 (1), 47–65.
- Das, N., 2007. Modeling Three-Dimensional Shape of Sand Grains Using Discrete Element Method (Ph.D. thesis). University of South Florida.
- Di Renzo, A., Di Maio, F.P., 2005. An improved integral non-linear model for the contact of particles in distinct element simulations. *Chem. Eng. Sci.* 60 (5), 1303–1312.
- Duriez, J., Bonelli, S., 2021. Precision and computational costs of Level Set-Discrete Element Method (LS-DEM) with respect to DEM. *Comput. Geotech.* 134, 104033.
- Faramarzi, L., Kheradmandian, A., Azhari, A., 2020. Evaluation and Optimization of the Effective Parameters on the Shield TBM Performance: Torque and Thrust – Using Discrete Element Method (DEM). *Geotech. Geol. Eng.* 1–15.
- Feldfogel, K., Andrade, J., Kammer, D.S., 2023. A discretization-convergent level-set-discrete-element-method using a continuum-based contact formulation. *Internat. J. Numer. Methods Eng.* e7400.
- Feng, Y.T., 2021a. An energy-conserving contact theory for discrete element modelling of arbitrarily shaped particles: Basic framework and general contact model. *Comput. Methods Appl. Mech. Eng.* 373, 113454.
- Feng, Y.T., 2021b. An energy-conserving contact theory for discrete element modelling of arbitrarily shaped particles: Contact volume based model and computational issues. *Comput. Methods Appl. Mech. Eng.* 373, 113493.
- Harmon, J.M., Arthur, D., Andrade, J.E., 2020. Level set splitting in DEM for modeling breakage mechanics. *Comput. Methods Appl. Mech. Eng.* 365, 112961.

- Hart, R., Cundall, P.A., Lemos, J., 1988. Formulation of a three-dimensional distinct element model—Part II. Mechanical calculations for motion and interaction of a system composed of many polyhedral blocks. *Int. J. Rock Mech. Min. Sci. Geomech. Abstr.* 25 (3), 117–125.
- van der Haven, D.L.H., Fragkopoulou, L.S., Elliott, J.A., 2023. A physically consistent discrete element method for arbitrary shapes using volume-interacting level sets. *Comput. Methods Appl. Mech. Engrg.* 414, 116165.
- Hertz, H., 1882. Ueber die Berührung fester elastischer Körper (On the contact of elastic solids). *J. Reine Angew. Math.* 92, 156–171.
- Huang, S., Huang, L., Lai, Z., Zhao, J., 2023. Morphology characterization and discrete element modeling of coral sand with intraparticle voids. *Eng. Geol.* 315, 107023.
- Johnson, K.L., 1987. *Contact Mechanics*. Cambridge University Press.
- Kawamoto, R., Andò, E., Viggiani, G., Andrade, J.E., 2016. Level set discrete element method for three-dimensional computations with triaxial case study. *J. Mech. Phys. Solids* 91, 1–13.
- Kawamoto, R., Andò, E., Viggiani, G., Andrade, J.E., 2018. All you need is shape: Predicting shear banding in sand with LS-DEM. *J. Mech. Phys. Solids* 111, 375–392.
- Lai, Z., Zhao, S., Zhao, J., Huang, L., 2022. Signed distance field framework for unified DEM modeling of granular media with arbitrary particle shapes. *Comput. Mech.* 70 (4), 763–783.
- Lai, Z., Zhao, J., Zhao, S., Huang, L., 2023. Signed distance field enhanced fully resolved CFD-DEM for simulation of granular flows involving multiphase fluids and irregularly shaped particles. *Comput. Methods Appl. Mech. Engrg.* 414, 116195.
- Li, L., Marteau, E., Andrade, J.E., 2019. Capturing the inter-particle force distribution in granular material using LS-DEM. *Granul. Matter* 21, 1–16.
- Li, Y., Xu, Y., Thornton, C., 2005. A comparison of discrete element simulations and experiments for ‘sandpiles’ composed of spherical particles. *Powder Technol.* 160 (3), 219–228.
- Lim, K.-W., Andrade, J.E., 2014. Granular element method for three-dimensional discrete element calculations. *Int. J. Numer. Anal. Methods Geomech.* 38 (2), 167–188.
- Malone, K.F., Xu, B.H., 2008. Determination of contact parameters for discrete element method simulations of granular systems. *Particuology* 6 (6), 521–528.
- Martys, N.S., Mountain, R.D., 1999. Velocity Verlet algorithm for dissipative-particle-dynamics-based models of suspensions. *Phys. Rev. E* 59 (3), 3733.
- Mollon, G., Zhao, J., 2014. 3D generation of realistic granular samples based on random fields theory and Fourier shape descriptors. *Comput. Methods Appl. Mech. Engrg.* 279, 46–65.
- Moncada, R., Gupta, M., Thompson, A., Andrade, J.E., 2023. Level set discrete element method for modeling sea ice floes. *Comput. Methods Appl. Mech. Engrg.* 406, 115891.
- Mударisov, S., Farkhutdinov, I., Khamaletdinov, R., Khasanov, E., Mukhametdinov, A., 2022. Evaluation of the significance of the contact model particle parameters in the modelling of wet soils by the discrete element method. *Soil Tillage Res.* 215, 105228.
- Muth, B., Müller, M.-K., Müller, M., Eberhard, P., Luding, S., 2007. Collision detection and administration methods for many particles with different sizes. In: 4th International Conference on Discrete Element Methods, DEM 4. Minerals Engineering Int., pp. 1–18.
- O’Sullivan, C., Bray, J.D., 2004. Selecting a suitable time step for discrete element simulations that use the central difference time integration scheme. *Eng. Comput.*
- Otsubo, M., O’Sullivan, C., Shire, T., 2017. Empirical assessment of the critical time increment in explicit particulate discrete element method simulations. *Comput. Geotech.* 86, 67–79.
- Rackl, M., Hanley, J., 2017. A methodical calibration procedure for discrete element models. *Powder Technol.* 307, 73–83.
- Rojek, J., Labra, C., Su, O., Oñate, E., 2012. Comparative study of different discrete element models and evaluation of equivalent micromechanical parameters. *Int. J. Solids Struct.* 49 (13), 1497–1517.
- Shi, X.S., Liu, K., Yin, J., 2021. Effect of initial density, particle shape, and confining stress on the critical state behavior of weathered gap-graded granular soils. *J. Geotech. Geoenviron. Eng.* 147 (2), 04020160.
- Thornton, C., 2000. Numerical simulations of deviatoric shear deformation of granular media. *Géotechnique* 50 (1), 43–53.
- Thornton, C., Cummins, S.J., Cleary, P.W., 2011. An investigation of the comparative behaviour of alternative contact force models during elastic collisions. *Powder Technol.* 210 (3), 189–197.
- Tu, X., Andrade, J., 2008. Criteria for static equilibrium in particulate mechanics computations. *Int. J. Numer. Methods Eng.* 75 (13), 1581–1606.
- Wachs, A., Girolami, L., Vinay, G., Ferrer, G., 2012. Grains3D, a flexible DEM approach for particles of arbitrary convex shape – Part I: Numerical model and validations. *Powder Technol.* 224, 374–389.
- Wang, S., Ji, S., 2022. A unified level set method for simulating mixed granular flows involving multiple non-spherical DEM models in complex structures. *Comput. Methods Appl. Mech. Engrg.* 393, 114802.
- Wang, Y., Li, L., Hofmann, D., Andrade, J.E., Daraio, C., 2021. Structured fabrics with tunable mechanical properties. *Nature* 596 (7871), 238–243.
- Wu, M., Wang, J., Russell, A., Cheng, Z., 2021. DEM modelling of mini-triaxial test based on one-to-one mapping of sand particles. *Géotechnique* 71 (8), 714–727.
- Zhao, S., Zhao, J., 2023. Revolutionizing granular matter simulations by high-performance ray tracing discrete element method for arbitrarily-shaped particles. *Comput. Methods Appl. Mech. Engrg.* 416, 116370.
- Zhou, Z., Andreini, M., Sironi, L., Lestuzzi, P., Andò, E., Dubois, F., Bolognini, D., Dacarro, F., Andrade, J.E., 2023. Discrete structural systems modeling: Benchmarking of LS-DEM and LMGC90 with seismic experiments. *J. Eng. Mech.* 149 (12), 04023097.
- Zhou, B., Wang, J., 2017. Generation of a realistic 3D sand assembly using X-ray micro-computed tomography and spherical harmonic-based principal component analysis. *Int. J. Numer. Anal. Methods Geomech.* 41 (1), 93–109.
- Zhou, B., Wang, J., Wang, H., 2018. A novel particle tracking method for granular sands based on spherical harmonic rotational invariants. *Géotechnique* 68 (12), 1116–1123.
- Zhou, B., Wang, J., Zhao, B., 2015. Micromorphology characterization and reconstruction of sand particles using micro X-ray tomography and spherical harmonics. *Eng. Geol.* 184, 126–137.